Radio Astronomy

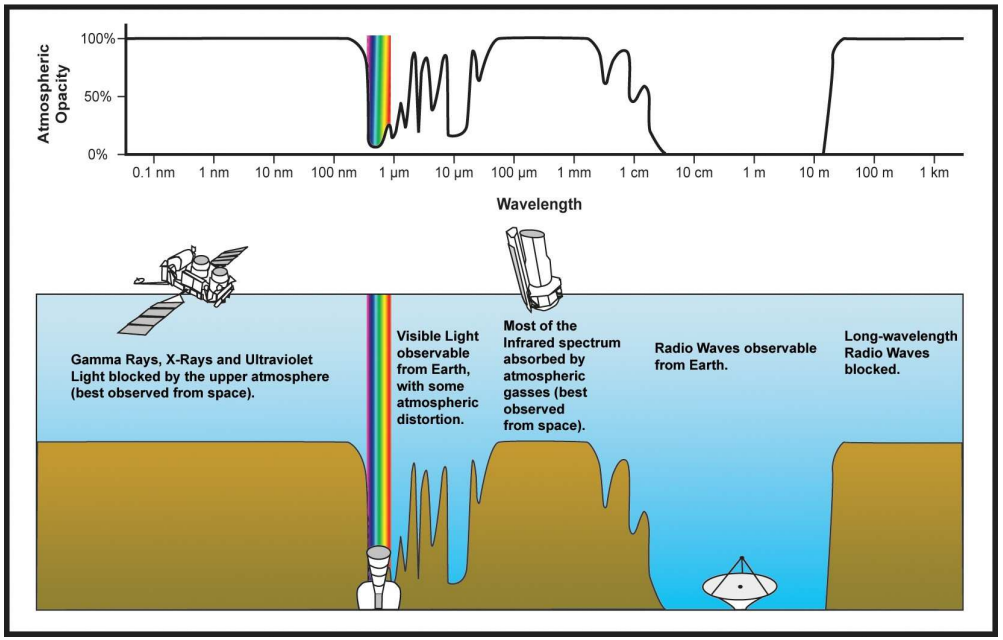

http://www.astro.psu.edu/%7Ekluhman/guide.html

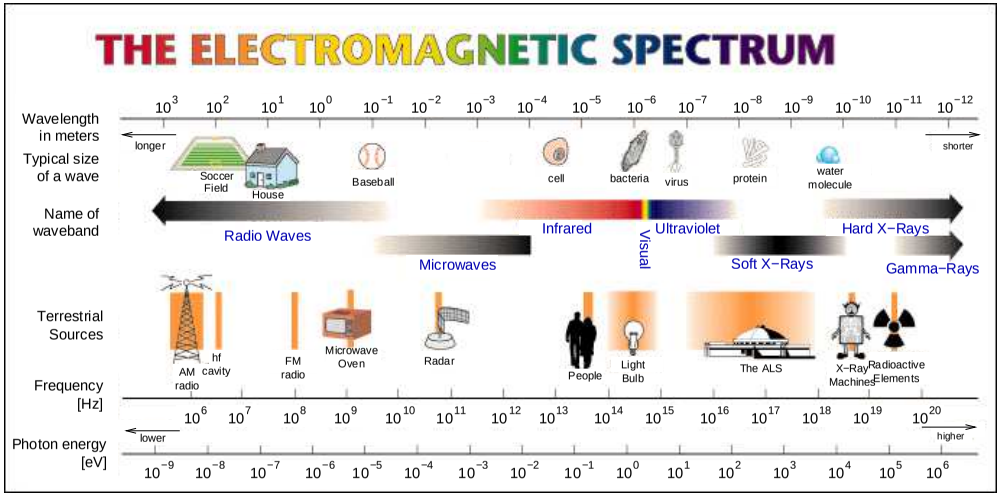

The Radio-Window in the Electromagnetic Spectrum, III

Reminder: all forms of light can be characterized by

Wavelength: λ, in the radio: mm to km.

Frequency: ν, in the radio: MHz to THz.

Energy: E, in the radio: neV to meV.

Remember:

$$\lambda\nu = c \quad \Rightarrow \quad \frac{\lambda}{[1\,\mathrm{cm}]} \times \frac{\nu}{[1\,\mathrm{GHz}]} \sim 30 \tag{6.1}$$

For example:

$$2\,\mathrm{cm} \mathrel{\hat{=}} 15\,\mathrm{GHz}$$
$$6\,\mathrm{cm} \mathrel{\hat{=}} 5\,\mathrm{GHz}$$
$$21\,\mathrm{cm} \mathrel{\hat{=}} 1.4\,\mathrm{GHz}$$

The Radio-Window in the Electromagnetic Spectrum, IV

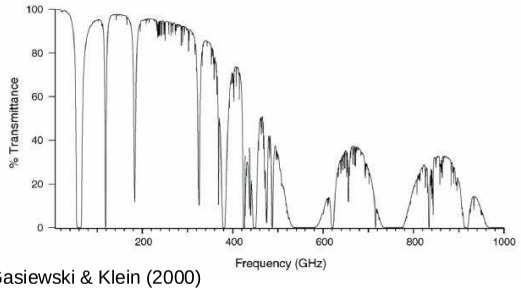

Gasiewski & Klein (2000)

L band: ∼1.4 GHz ≙ 21 cm
S band: ∼2.3 GHz ≙ 21 cm
C band: ∼5 GHz ≙ 6 cm
X band: ∼8.4 GHz ≙ 3.6 cm
Ku (U) band: ∼15 GHz ≙ 2 cm
K band: ∼23 GHz ≙ 1.3 cm
Q band: ∼43 GHz ≙ 7 mm
W band: ∼86 GHz ≙ 3 mm

15 MHz to 50 GHz largely transparent (dip at 22 GHz due to water vapor).

High-frequency windows at ∼3 mm (65–115 GHz), ∼2 mm (125–180 GHz), and ∼1.2 mm (200–300 GHz) and submillimeter windows.

Some important band-associated phenomena: 21 cm line, OH maser (L band), H_2O maser (K band), SiO maser (Q band)

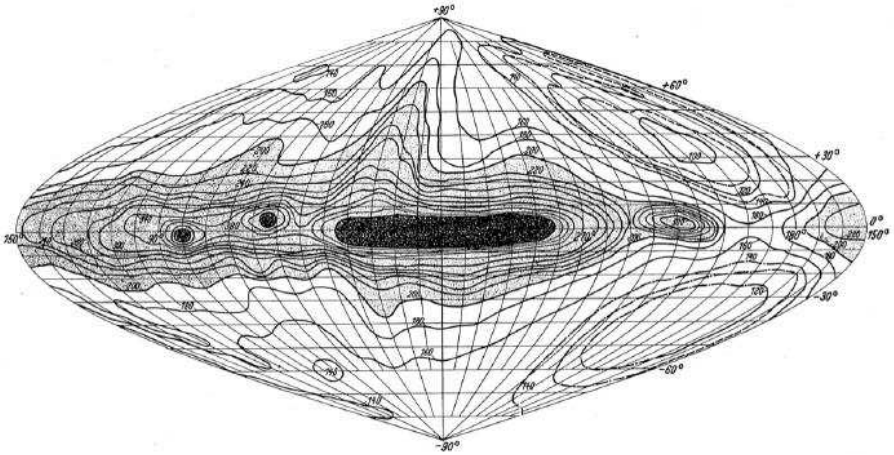

One of the first radio all-sky maps: 200 MHz, Dröge & Priester 1956

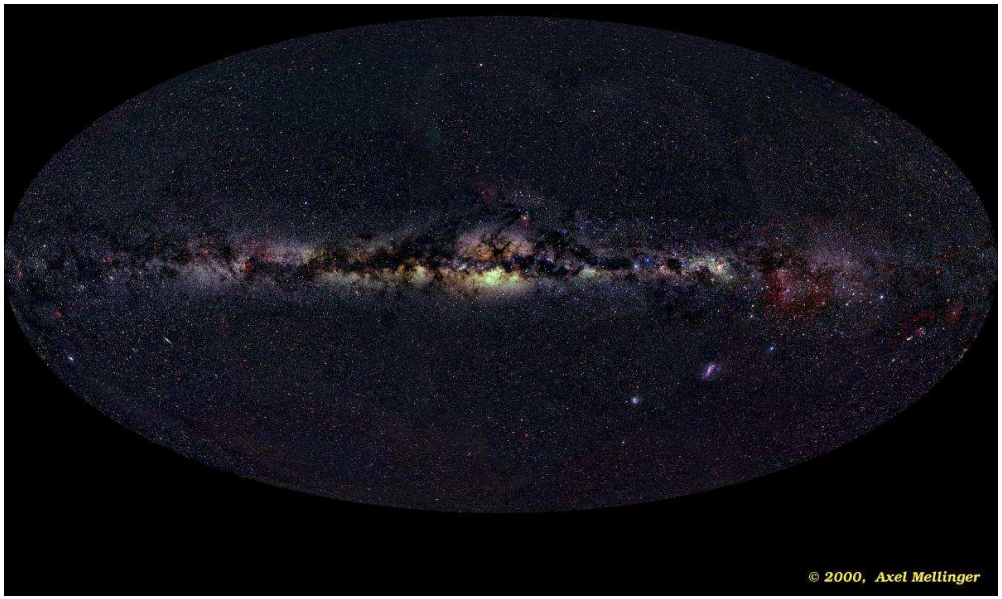

The Optical Sky

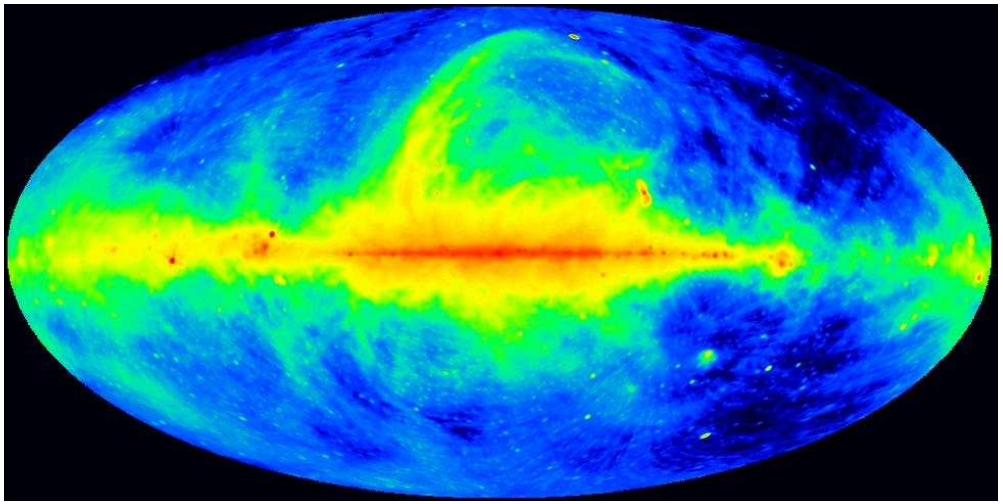

G.T. Haslam et al., MPI für Radioastronomie 1982

The radio sky ($\lambda = 73$ cm, $\nu = 408$ MHz) measured with the three antennas in Jodrell Bank (GB), Effelsberg (Germany) and Parkes (Australia).

No stars! Galactic plane (e.g., Pulsars, SNRs),

The Radio vs. the Optical Sky, IV

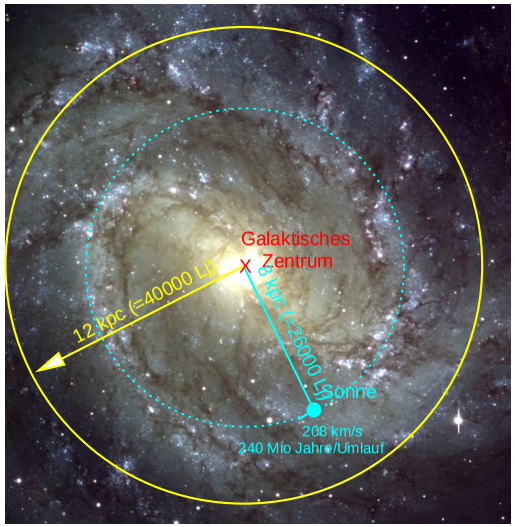

M83: ESO [VLT ANTU+FORS1]

The milky way as a galaxy:
Luminosity: $\sim 2 \times 10^{10}\, L_\odot$
Mass: $\sim 10^{11}\, M_\odot$ (visible)
$\sim 10^{12}\, M_\odot$ (all)
Stellar density: $\sim 0.3\, M_\odot\,\mathrm{pc}^{-3}$

$1\, M_\odot = 2 \times 10^{33}\,\mathrm{g} = 2 \times 10^{30}\,\mathrm{kg}$,
$1\, L_\odot = 4 \times 10^{33}\,\mathrm{erg\,s}^{-1} = 4 \times 10^{26}\,\mathrm{W}$

The Radio vs. the Optical Sky, V

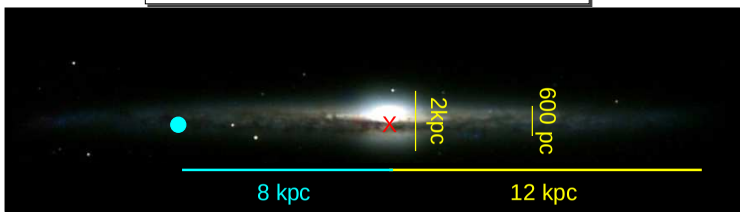

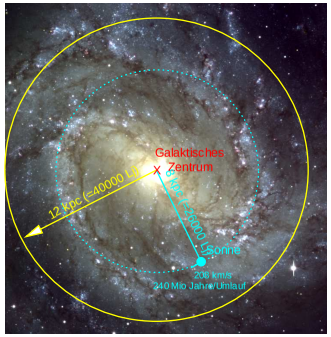

NGC 4565: W. McLaughlin

The milky way as a galaxy:
Luminosity: $\sim 2 \times 10^{10}\, L_\odot$
Mass: $\sim 10^{11}\, M_\odot$ (visible)
$\sim 10^{12}\, M_\odot$ (all)
Stellar density: $\sim 0.3\, M_\odot\,\mathrm{pc}^{-3}$

$1\, M_\odot = 2 \times 10^{33}\,\mathrm{g} = 2 \times 10^{30}\,\mathrm{kg}$,
$1\, L_\odot = 4 \times 10^{33}\,\mathrm{erg\,s}^{-1} = 4 \times 10^{26}\,\mathrm{W}$

The Radio vs. the Optical Sky, VI

Most stars seen within $\sim 1\,\mathrm{kpc}$

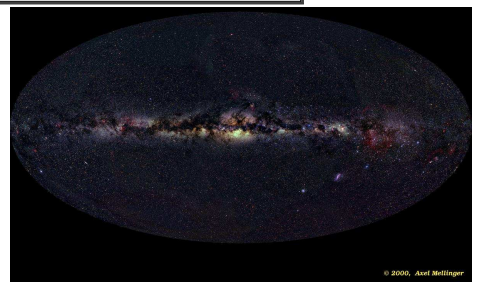

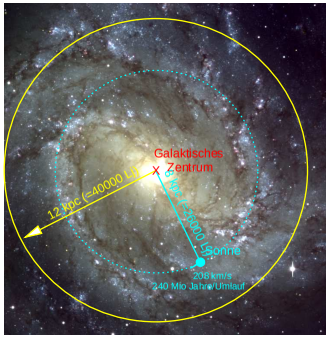

The milky way as a galaxy:
Luminosity: $\sim 2 \times 10^{10}\, L_\odot$
Mass: $\sim 10^{11}\, M_\odot$ (visible)
$\sim 10^{12}\, M_\odot$ (all)
Stellar density: $\sim 0.3\, M_\odot\,\mathrm{pc}^{-3}$

$1\, M_\odot = 2 \times 10^{33}\,\mathrm{g} = 2 \times 10^{30}\,\mathrm{kg}$,
$1\, L_\odot = 4 \times 10^{33}\,\mathrm{erg\,s}^{-1} = 4 \times 10^{26}\,\mathrm{W}$

The Radio vs. the Optical Sky, VII

Milky way transparent in radio

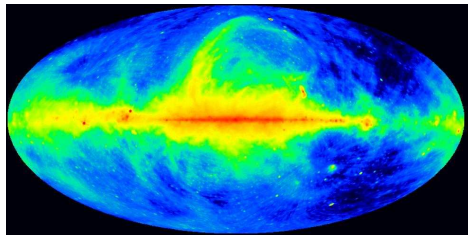

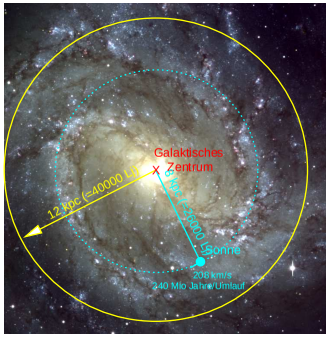

The milky way as a galaxy:
Luminosity: $\sim 2 \times 10^{10}\, L_\odot$
Mass: $\sim 10^{11}\, M_\odot$ (visible)
$\sim 10^{12}\, M_\odot$ (all)
Stellar density: $\sim 0.3\, M_\odot\,\mathrm{pc}^{-3}$

$1\, M_\odot = 2 \times 10^{33}\,\mathrm{g} = 2 \times 10^{30}\,\mathrm{kg}$,
$1\, L_\odot = 4 \times 10^{33}\,\mathrm{erg\,s}^{-1} = 4 \times 10^{26}\,\mathrm{W}$

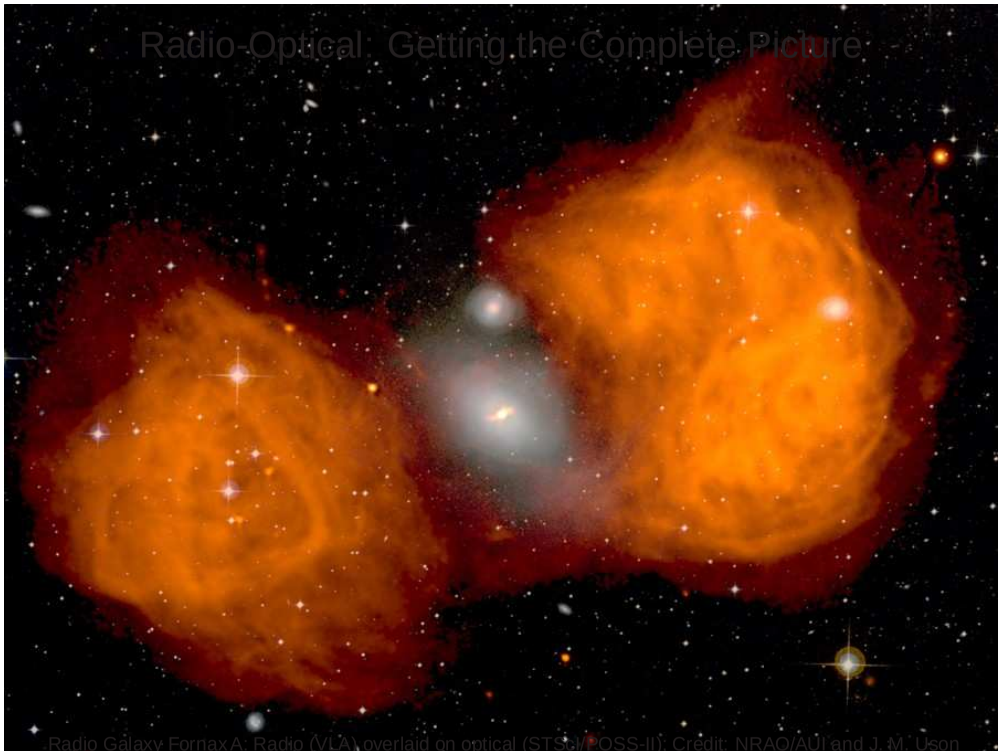

Radio Galaxy Fornax A: Radio (VLA) overlaid on optical (STScI/POSS-II). Credit: NRAO/AUI and J.M. Uson

The Birth of Radio Astronomy

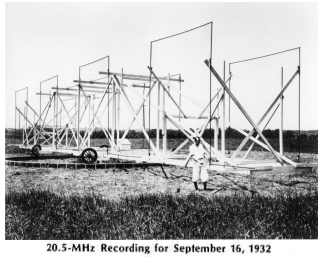

20.5-MHz Recording for September 16, 1932

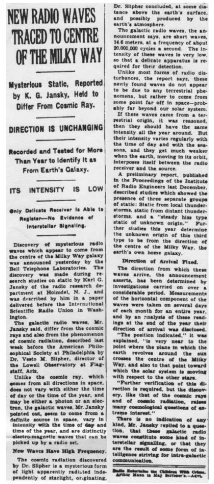

NEW RADIO WAVES TRACED TO CENTRE OF THE MILKY WAY

Mysterious Static, Reported by K. G. Jansky, Held to Differ From Cosmic Ray.

DIRECTION IS UNCHANGING

Recorded and Tested for More Than Year to Identify It as From Earth's Galaxy.

ITS INTENSITY IS LOW

Only Delicate Receiver Is Able to Register—No Evidence of Interstellar Signaling.

Karl Jansky (1905 – 1950) discovers 1931 the milky way radio emission

The Radio vs. the Optical Sky, IX

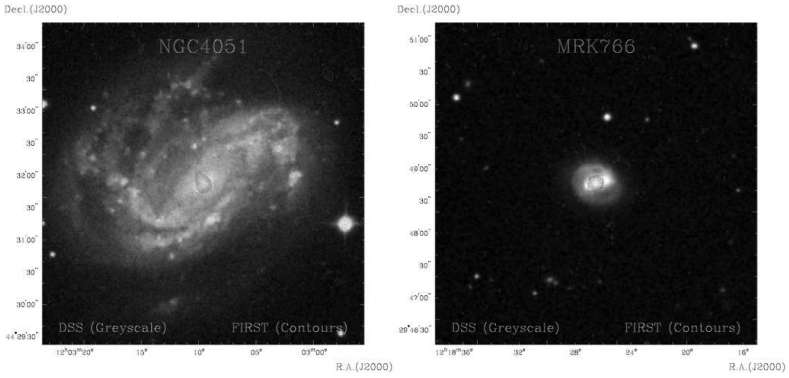

grey: optical; contours: radio (M. Kadler)

Seyfert Galaxies: optically detected and classified AGN.

Compact radio cores point to the active nucleus.

Overview

- Radio telescopes come in many shapes and sizes!
- Most important: sensitivity and angular resolution.
- Most universal type: steerable parabolic dishes. Alternatives: phased or interferometric arrays (next lecture).

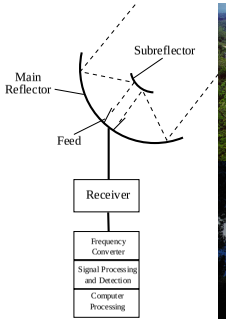

Parabolic Reflectors, I

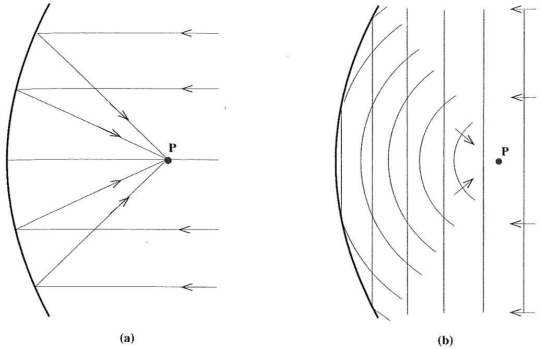

Focusing in terms of ray optics (a) or wavefronts (b). Fig.4.1. from Burke & Graham-Smith (2002).

A parabolic dish focuses incoming radiation at the focus.

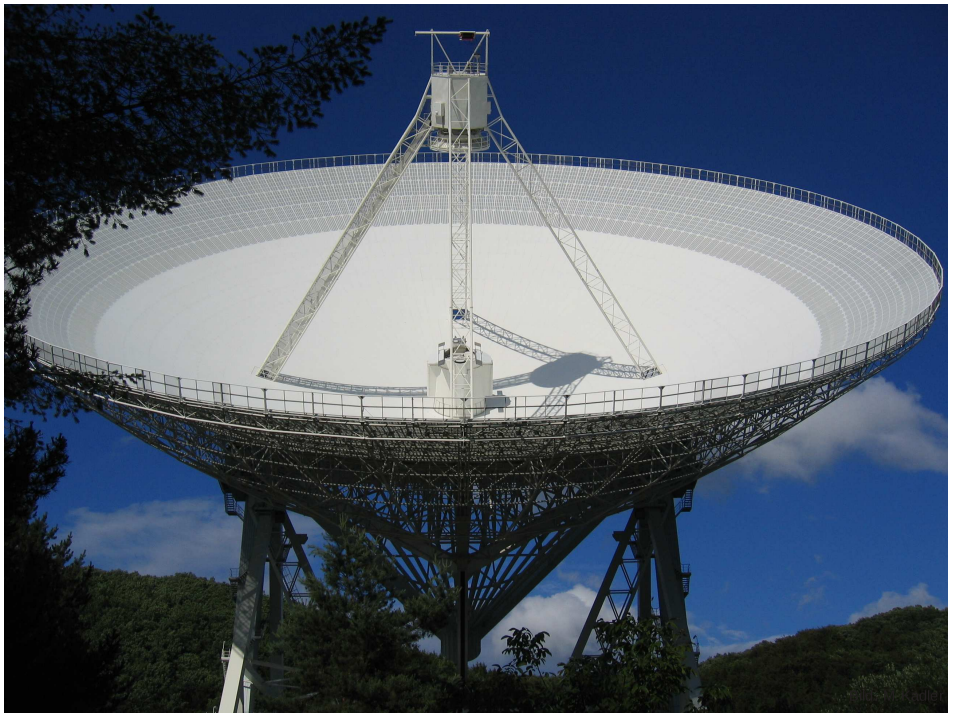

The Effelsberg 100-m Telescope

Parabolic Reflectors, II

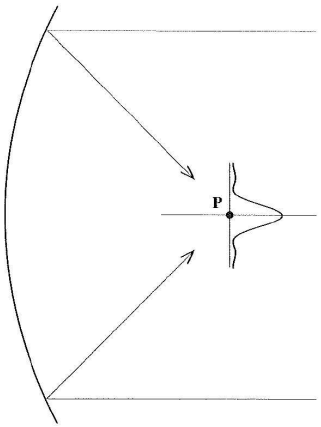

Fig.4.2. from Burke & Graham-Smith (2002).

All parts of a plane wave front arrive at the focal point in phase.
Analogous to a circular-aperture diffraction image in optics: Airy disc

Angular Resolution:
$$\theta \sim 0.42' \frac{\lambda}{[1\,\mathrm{cm}]} / \frac{D}{[100\,\mathrm{m}]}$$

$\theta \sim 9'$ for a 100-m dish observing at 21 cm, nine times worse than the naked eye at optical wavelengths!

Radio waves are 100000 times longer than optical waves ⇒ Radio Telescopes must be big!

Point-source response is known as the beam; its size is the beamwidth.

- Located near Bad Münstereifel, Germany; Built between 1968 and 1971
- Operated by the Max-Planck-Institut für Radioastronomie
- Diameter of reflecting dish: 100 m
- Total collecting area: 7850 m^2 (soccer field!)
- Weight: 3200 tons
- Observing wavelengths: 3 mm to 35 cm
- *Homology* design, i.e., the dish retains its parabolic shape when tilted

Until 2002, the largest steerable dish in the world; today, still the *powerhorse* in VLBI arrays and one of the best

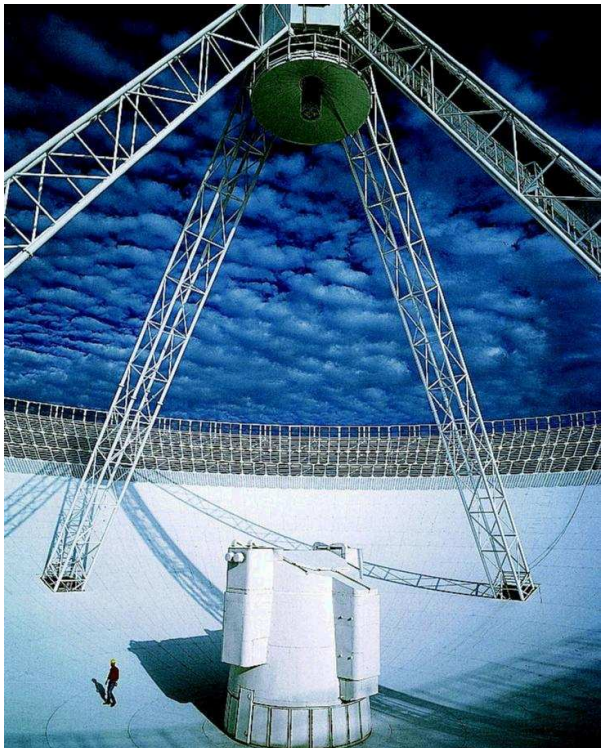

- 6.5 m subreflector 30 m above the primary focus reflects radiation into the secondary focus (Gregory system)
- New subreflector in 2006 with active surface; corrects surface inaccuracies of the primary mirror
- 3 mm observations in the secondary focus now possible

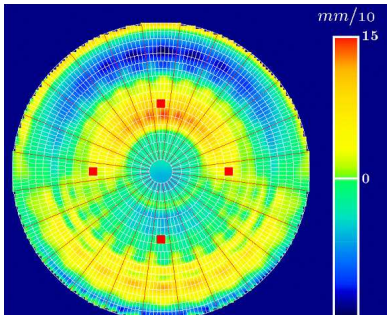

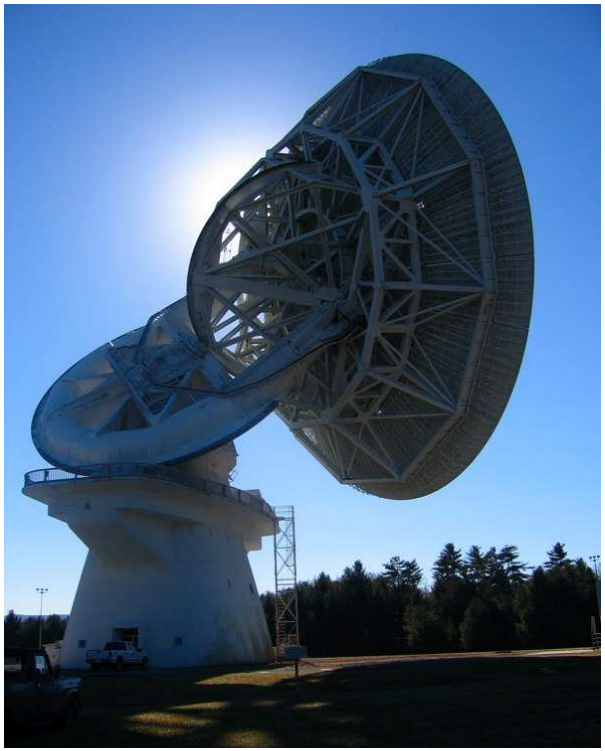

The NRAO 140-foot telescope is the only large radio telescope with a polar mount.

- Advantages: Tracking Simplicity (declination axis stays fixed, only hour-angle is tracked).
- Disadvantages: Mechanical stability is a challenge; expensive; heavy.

No longer in operation.

Construction delays of the 140-ft were the reasons for building a simpler and inexpensive, but really large dish at NRAO Green Bank: the 300-ft Green Bank telescope.

- Multiple feed receivers in the secondary focus
- Change of observing frequency possible within $\sim$ 30 sec

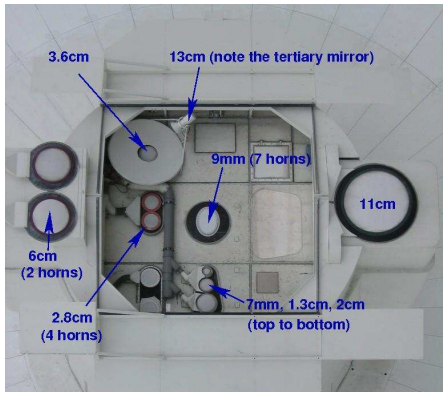

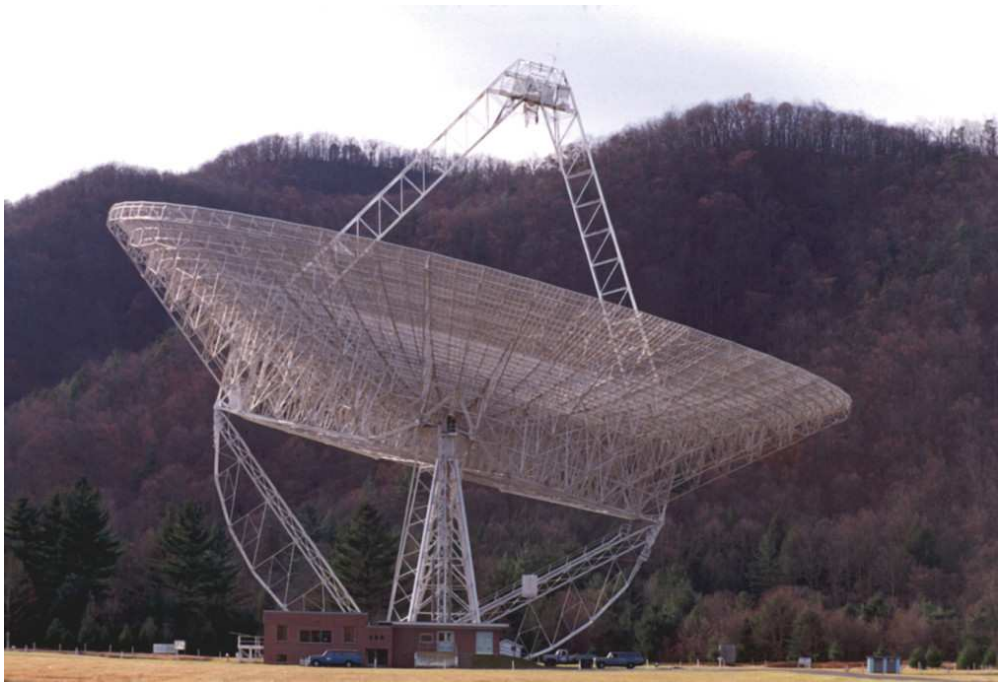

The NRAO 300-Foot Green Bank Telescope (Image R. Porcas, Nov 14, 1988)

The NRAO 300-Foot Green Bank Telescope (Image R. Porcas, Nov 15, 1988)

America's most powerful radio telescope IS . . .

ZAPPED!

. . . by hostile space aliens!

BEFORE ▲ AFTER ▶

THE Green Bank radio telescope in West Virginia after the alien attack. At left is how it looked after construction.

Space aliens zapped the enormous radio telescope at Green Bank, W. Va., with a powerful laser to keep scientists from monitoring their activities in the northern hemisphere!

That's the claim of Swiss astronomer Peter Voisard, who says the destruction of the 300-foot instrument on November 15 qualifies as the boldest act of extraterrestrial aggression in the history of the world.

By RAGAN DUNN

"We know that extraterrestrials have shot down planes and abducted people but this is the first time they have been brazen enough to destroy a government research facility," the expert told newsmen in Geneva. "The Americans must have been learning too much about them," he continued. "There is no other rational explanation for such a strike as this. In some circles it might be considered an act of war."

Dr. Voisard's report sent shockwaves throughout the world's scientific community. But the handful of men who can talk about the Green Bank disaster with authority refused to describe the incident as anything more than "a mystery."

There is no doubt that the instrument — which could detect objects almost two-thirds of the way to the edge of the visible universe — was essential to monitoring extraterrestrial activity in the northern skies.

And its devastation by a destructive beam stands as compelling proof that it was zapped by extraterrestrials who wanted to mask their activity from mankind, Dr. Voisard said.

"Any other explanation defies logic," he continued. "The telescope had been in operation since 1962 and was solid as a rock.

"Suddenly it collapses in the dead of night. What are we supposed to think? That the telescope just fell apart?"

French radio astronomer Marc Kraemer was inclined to agree with Dr. Voisard but warned against jumping to conclusions.

"I firmly believe that we can prove extraterrestrials toppled the telescope at Green Bank," he said. "But let's wait until all the evidence is in.

"Then we can take whatever steps are necessary to prevent things like this from happening in the future."

US Newspaper Article ca. 1988

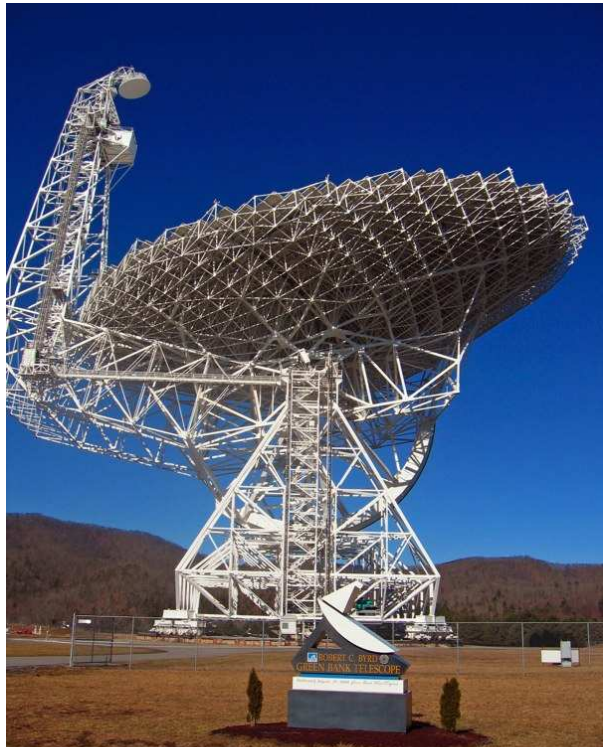

- The 300-ft collapse, eventually led to the construction of the new Green Bank Telescope (GBT).
- Completed in 2002
- 7300 tons
- The 110 m × 100 m dish is an asymmetrical section of a virtual 208 m paraboloid.
- Focus of the 208 m paraboloid is 4 m offset from the edge of the actual reflector. ⇒ Focal-arm does not block the aperture.

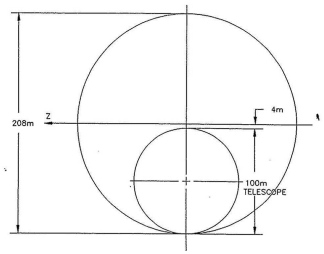

Theory of Radio Antennas

An antenna is the interface between a free-space electromagnetic radio wave and a guided wave.

The antenna pattern is the response of an antenna as a function of direction.

Reciprocity Theorem: An antenna can be treated either as a receiving device or as a transmitting system.

The reciprocity theorem follows directly from Maxwell's equations.

The power gain of an antenna in transmission is closely related to the effective area in reception.

Some large radio telescopes have been very successfully been used in radar experiments, e.g., planetary surface studies or imaging of space debris.

Theory of Radio Antennas

In receiving mode, an antenna intercepts an incoming power flux S, yielding a received power $P_{\rm rec}$.

$$P_{\rm rec} = A_{\rm eff} S \tag{6.2}$$

$A_{\rm eff}$ is direction dependent (with respect to the antenna axis) and the range of directions over which it is large is called the antenna beamwidth.

The incoming power flux will in general come from a source with finite size emitting over a range of frequencies ν, whose specific brightness distribution $B_\nu(\theta, \phi)$ is defined as the flux per unit solid angle in the direction (θ, ϕ) at a given frequency. The total incoming flux is then given by

$$S = \iiint B_\nu(\theta, \phi)\, d^2\Omega\, d\nu \tag{6.3}$$

Considering a unit frequency interval leads to the specific flux or flux density S_ν, measured in units of $\mathrm{W\,m^{-2}\,Hz^{-1}}$.

$$1\,\mathrm{Jy} = 10^{-26}\,\mathrm{W\,m^{-2}\,Hz^{-1}}$$

The molecules of a resistor with the temperature T in an electrical circuit have a thermal energy, which gives rise to a thermal noise signal. This is a stochastical process, generating currents and voltages with a spectral noise power density of

$$n_0(\nu) = kT \quad , \tag{6.6}$$

which is constant over a wide frequency range (white noise).

Consider an antenna inside a black body of temperature T. From eq. 6.2 and eq. 6.3, the received power is

$$P_{\rm rec} = \frac{1}{2} A_{\rm eff} \frac{kT}{\lambda^2} \Omega_{\rm Ant} \tag{6.7}$$

because the specific intensity is given by the Rayleigh-Jeans approximation of the Planck formula for a black body with $B_\nu = 2kT/\lambda^2$. The factor $\frac{1}{2}$ considers that a typical antenna can only receive one polarisation direction, while the signal is assumed to be unpolarised. $\Omega_{\rm Ant}$ is the antenna beamwidth.

From the antenna theory (e.g. Burke & Graham-Smith, 2002) it can be shown that

$$\lambda^2 = A_{\rm eff} \Omega_{\rm eff} \tag{6.8}$$

so that

$$P_{\rm rec} = kT \quad . \tag{6.9}$$

Theory of Radio Antennas

The antenna temperature $T_{\rm Ant}$ is defined as the equivalent temperature of a resistor, which would create a noise signal (Johnson noise) in the receiver system of the same spectral power as the recorded signal $P_{\rm rec}$.

$$P_{\rm rec} = kT_{\rm Ant} \tag{6.4}$$

The telescope gain G quantifies the amount of radio noise power received from a source of unit flux density:

$$G \propto \frac{P_{\rm rec}}{S} \quad [\mathrm{K/Jy}] \tag{6.5}$$

The gain describes the overall quality of a receiving system.

The gain can be elevation dependent (e.g., gravitational deformations of the parabolic dish). For example, the gain of the Effelsberg 100-m telescope is 1.5 at 6 cm wavelength and 0.1 at 3 mm wavelength.

Theory of Radio Antennas

Another important quantity is the system temperature $T_{\rm sys}$.

$T_{\rm sys}$ is the antenna temperature measured in an idealized experiment in which the receiver noise and all background sources are considered (but no target source inside the antenna beam).

Main components of $T_{\rm sys}$ are

- Johnson noise from the receiver electronics
- *Spillover emission* can reach the feedhorn without being reflected from the parabolic dish (e.g., from the ground)
- The empty sky will give rise to a signal

$$T_{\rm sys} = T_{\rm receiver} + T_{\rm spillover} + T_{\rm sky}$$

A system temperature measurement is similar to a flat-field in optical astronomy.

Theory of Radio Antennas

- The actual process of converting the incoming signal into an electric noise signal happens at the antenna focus in a device called the feed via induced voltage oscillations in a special conductor.
- The simplest sort of feed is a linear dipole, which responds to E-field oscillations in a single plane. Other feeds may respond to a circular polarization mode.
- The output of a feed is the noise voltage, representing noise power from the radio source and measured as the antenna temperature, T_{Ant}.
- The backend amplifies and filters the noise signal (next lecture)

Theory of Radio Antennas

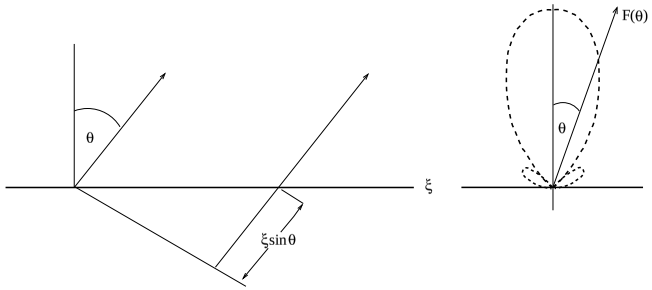

Radiation pattern in direction θ of a 1D line distribution along axis ξ with excitation currents $i(\xi)$ depends on the phase introduced by $\xi sin(\theta)$ (see Burke & Graham-Smith, 2002, for details).

$$F(\theta) = \int \exp(-i\,(2\pi\,\xi\,\theta/\lambda))\,i(\xi)\,d\xi \qquad (6.10)$$

The radiation pattern ($\hat{=}$ reception pattern) is the Fourier transform of the aperture distribution. Uniformly illuminated circular aperture $\Rightarrow$ sinc function.

Background, I

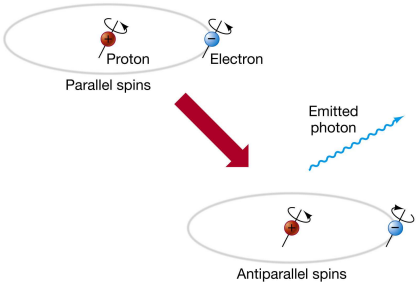

Image: 2005, Pearson Prentice Hall, Inc.

- Transition between two hyperfine levels of the ground state in the hydrogen atom.
- Spins of electron and proton may be parallel (F=1) or antiparallel (F=0); energy difference of $\Delta E \sim 6 \times 10^{-6}$ eV.
- F=1 is a metastable state, i.e., long life time (10^7 years); transition to F=0 *forbidden* in quantum mechanics, i.e., transition rate 10^{-6} smaller than for permitted transitions.
- In the laboratory, F=1 state is depopulated by collisions; energy goes into kinetic energy of the particles and no line is seen.
- In the ISM, low densities, i.e., no collisions; radiative transitions possible.

Background, II

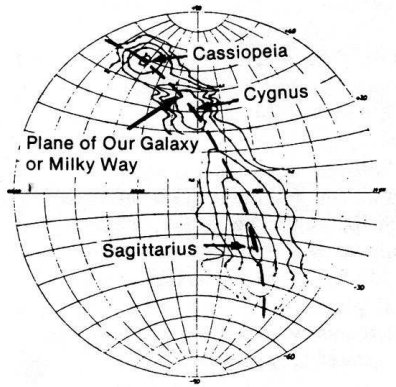

Reber's 1944 map of the radio sky

- Grote Reber built the first parabolic radio telescope (9 m, located in his back yard in Wheaton, Il) in 1937.
- Two papers published in ApJ in 1940 (Reber, 1940, 1944), identifying the milky way as the source of the brightest radio emission and presenting a sky map at 160 MHz (1.9 m).
- Jan Oort and Hendrick van de Hulst at Leiden Observatory realize that the detection of a radio spectral line would allow them to study the structure and dynamics of the milky way. Van de Hulst predicts the 21 cm line from the hydrogen hyperfine transition.
- Detection of the line in 1951 by Harold Ewen and Edward Purcell (Ewen & Purcell, 1951).

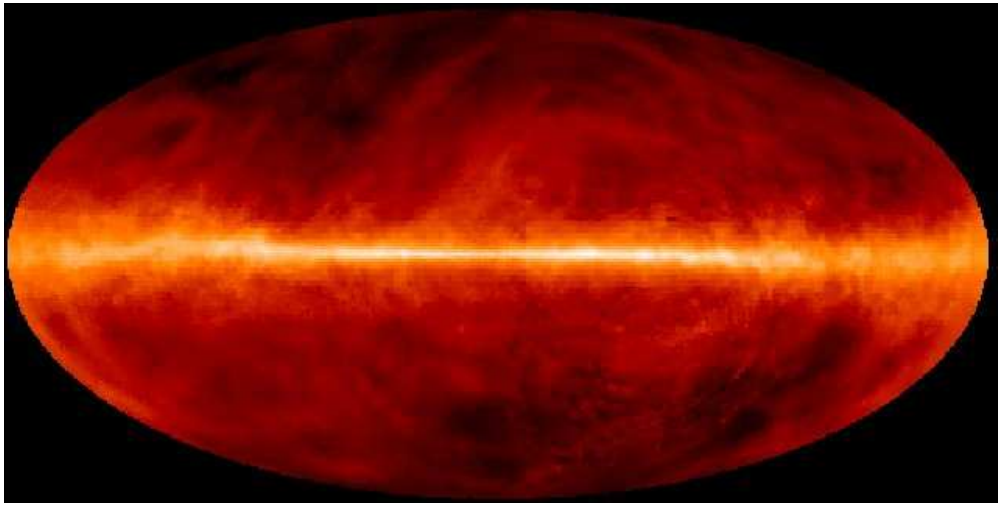

J. Dickey/F. Lockman/SkyView

Distribution of H I (λ=21 cm)

Most emission from inside the Galactic plane but substantial signal also at large Gal. latitudes.

Measuring Galactic Structure and Dynamics, I

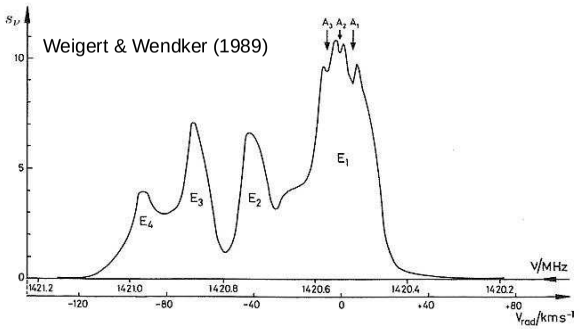

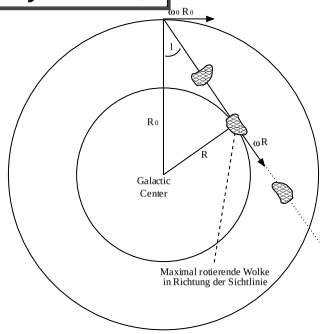

Sketch of a typical H I emission line profile around $\lambda = 21$ cm ($\nu = 1.4$ GHz). In general multiple hydrogen clouds along the line of sight. Differential rotation $\Rightarrow$ Differential Doppler shift; line width corresponds to cloud substructure and thermal broadening. Absorption components can be superimposed on the emission lines. Overall: Probe of ISM structure and dynamics!

Integration over the full profile gives the column density of neutral hydrogen in this direction. Typical values: 10^{18} cm^{-2} (at large gal. latitudes) to 10^{22} cm^{-2} (in the gal. plane).

State of the art is the LAB survey (Leiden-Argentine-Bonn Survey, Kalberla et al., 2005).

Measuring Galactic Structure and Dynamics, II

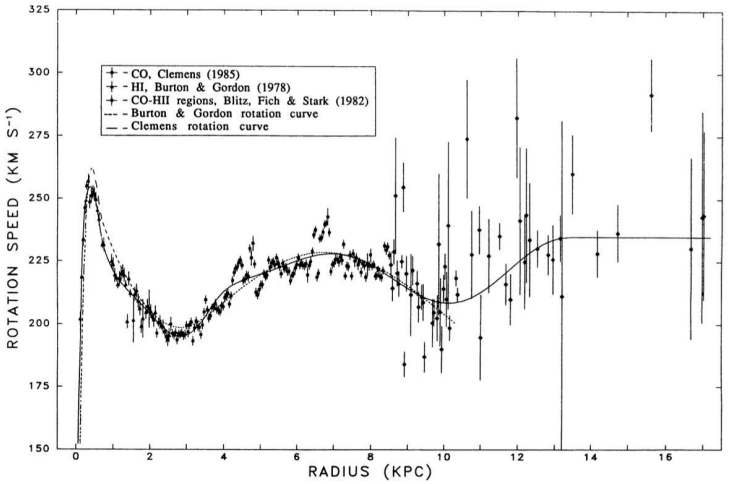

The rotation curve of the Galaxy (Combes, 1991)

Demo: The Bamberg Small Radio Telescope

- Located at the Dr. Remeis Sternwarte Bamberg
- Diameter 2.3 m
- L-band receiver ($\sim$ 1.4 GHz)
- Gain: $\sim$ 0.5 mK/Jy $\Rightarrow$ Main targets: sun, milky way, (Cas A), (Cyg A).
- Angular resolution: $\sim 6.4^\circ$
- Small sensitivity and large beam, but observing principles the same as for a 100-m dish; mainly used in the astronomy lab course.

Arecibo, I

The 100-m class represents a limit in maximum size for fully-steerable antennas. A further increase in sensitivity and angular resolution can only be achieved with interferometric techniques (next lecture) or if one gives up the concept of full steerability.

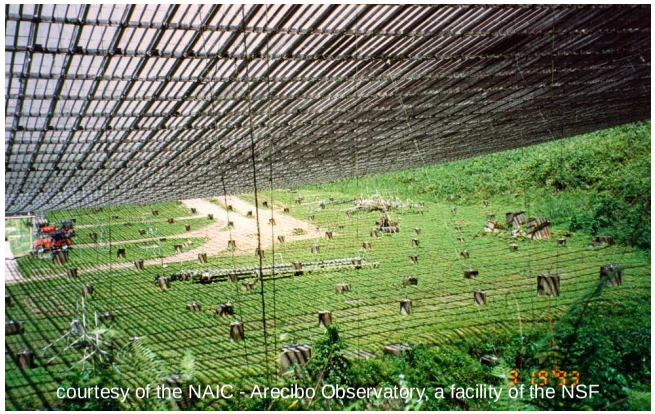

The biggest dishes 1

Arecibo Observatory Construction 1960-1963

courtesy of the NAIC - Arecibo Observatory, a facility of the NSF

Arecibo Observatory Construction 1960-1963

Arecibo Observatory Construction 1960-1963

Arecibo, VII

The Arecibo reflector is a segment of a sphere, not a parabloid! The focus is no longer a point but a line segment.

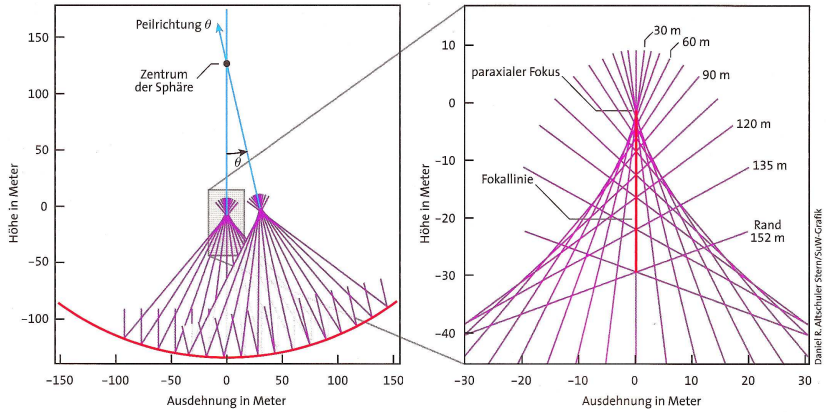

Arecibo Observatory Construction 1960-1963

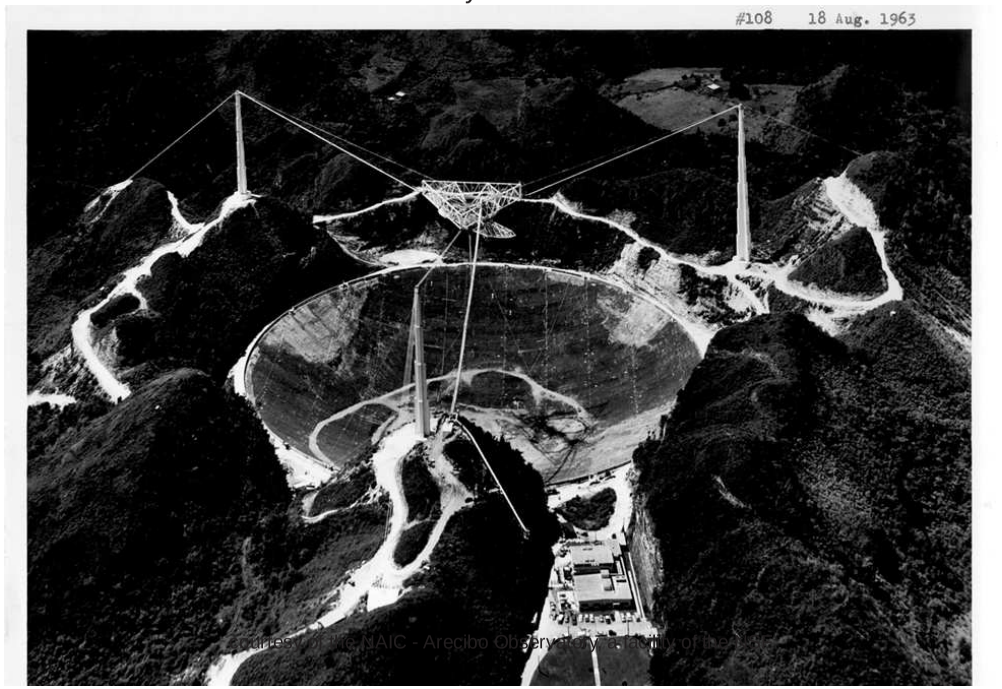


The old Arecibo Line Feed

Arecibo, IX

Since 2002, a secondary and tertiary mirror correct for the sphaeric abberation at Arecibo.

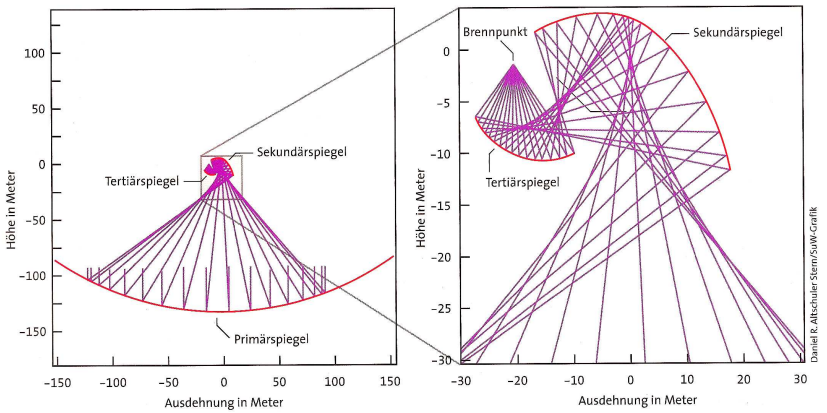

Burke, B. F., & Graham-Smith, F., 2002, An Introduction to Radio Astronomy: Second Edition

Combes, F., 1991, ARA&A, 29, 195

Ewen, H. I., & Purcell, E. M., 1951, Nature, 168, 356

Gasiewski, A. J., & Klein, M., 2000, Journal of Geophysical Research-Atmospheres, 13, 17481

Kalberla, P. M. W., Burton, W. B., Hartmann, D., Arnal, E. M., Bajaja, E., Morras, R., & Pöppel, W. G. L., 2005, 440, 775

Reber, G., 1940, ApJ, 91, 621

Reber, G., 1944, ApJ, 100, 279

Weigert, A., & Wendker, H. J., 1989, Astronomie und Astrophysik - ein Grundkurs.

FAST

Construction of the *Five-hundred-meter Aperture Spherical Telescope* (FAST) begun in January 2009.

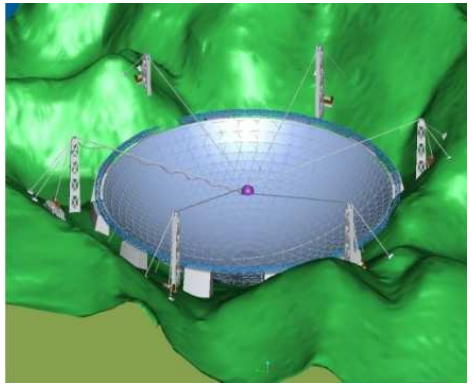

Image: Physicsworld.com

The Two-Element Interferometer, I

Remember:

Angular Resolution of a single radio dish:
$$\theta \sim 0.42' \frac{\lambda}{[1\,\mathrm{cm}]} \Big/ \frac{D}{[100\,\mathrm{m}]}$$

$\theta \sim 9'$ for a 100-m dish observing at 21 cm, nine times worse than the naked eye at optical wavelengths!

Radio interferometry increases D. $\Rightarrow$ Dramatic improvement of the angular resolution possible!

The following discussion is in a radio-astronomy context but can be applied to other wavelengths, as well. In practice, doing interferometry becomes more difficult toward shorter wavelengths.

The Two-Element Interferometer, II

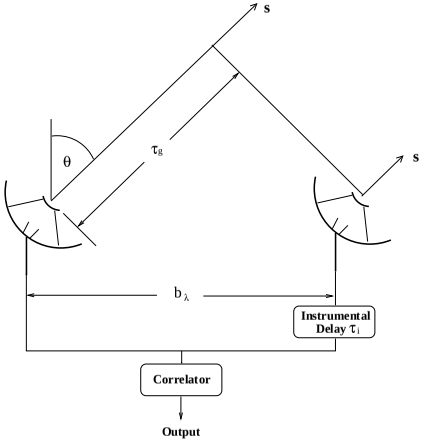

Geometry of a two-element interferometer.
After Burke & Graham-Smith (2002).

Basic concept:

- Signals of two antennas are added, amplified and detected.
- Superposition will result in either constructive or destructive interference, depending on the geometrical delay τ_g and the instrumental delay τ_i.
- While the earth rotates, τ_g is sinusoidally modulated ⇒ Fringes in the time domain.
- Interferometer output can be characterized as a complex quantity with amplitude (amplitude between constructive and destructive interference) and a phase.

The Two-Element Interferometer, III

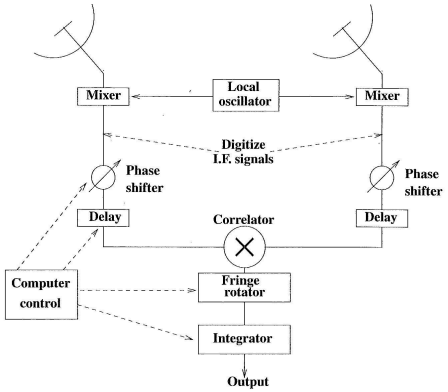

Burke & Graham-Smith (2002)

Signal from the antennas (ν_0 in the GHz range) is first mixed with a signal from a *local oscillator*. Multiplication yields

$$\nu_{\mathrm{if}} = \nu_0 \pm \nu_{\mathrm{lo}} \quad . \tag{6.11}$$

If ν_{lo} is close to ν_0, then the *intermediate frequency* in the lower sideband is much smaller and easier to transmit and to correlate.

This concept is called *heterodyne receiver.*

The Two-Element Interferometer, IV

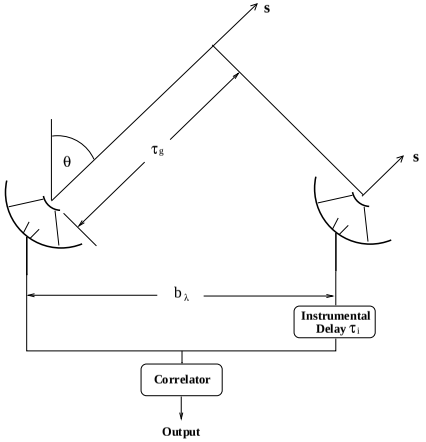

Geometry of a two-element interferometer.
After Burke & Graham-Smith (2002).

Set $\tau_i = 0$. Signal arrives at second antenna with a geometrical time delay:

$$\tau_g = \mathbf{b} \cdot \mathbf{s}/c = (b/c)\sin\theta \tag{6.12}$$

Feeding the signals into a voltage multiplier corresponds to a cross-correlation:

$$R_{x,y}(\tau_g) = \langle x(t)\, y(t-\tau_g)\rangle \tag{6.13}$$

$R_{x,y}$ has the dimensions of power and is called the cross-power product.

Assume monochromatic signal at frequency ν:

$$\begin{aligned} x(t) &= V\cos(2\pi\nu t) \\ y(t) &= V\cos(2\pi\nu[t-\tau_g]) \end{aligned}$$

Thus:

$$R_{x,y}(\tau_g) = A(\mathbf{s})\, S\, \cos(2\pi\nu\tau_g) \tag{6.14}$$

since the power received from the source must be proportional to the effective area $A(\mathbf{s})$ and the source flux S.

The Two-Element Interferometer, V

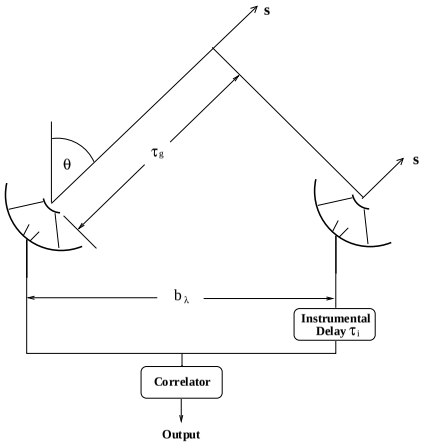

Geometry of a two-element interferometer.
After Burke & Graham-Smith (2002).

Express the baseline in terms of units of wavelength

$$\mathbf{b}_\lambda = \mathbf{b}/\lambda \quad . \tag{6.15}$$

The correlator output is then

$$R_{x,y}(\tau_g) = A(\mathbf{s})\, S\, \cos(2\pi\mathbf{b}_\lambda \cdot \mathbf{s}) \quad . \tag{6.16}$$

For small angles θ, the modulation is approximately sinusoidal since $\mathbf{b}/\lambda \cdot \mathbf{s} \sim b_\lambda\,\theta$:

$$R_{x,y}(\tau_g) = A(\mathbf{s})\, S\, \cos(2\pi\, b_\lambda\theta) \quad . \tag{6.17}$$

The response of a two-element interferometer to a monochromatic point source is the response of a single antenna modulated with a sinusoidal fringe pattern over the antenna beam. The individual fringes are separated by $\sim 1/b_\lambda$.

Eq. 6.16 can be expressed in a complex representation:

$$S_{x,y}(\mathbf{s}) = A(\mathbf{s})\, S\, \exp(i2\pi\,\mathbf{b}_\lambda \cdot \mathbf{s}) \quad . \tag{6.18}$$

Effects of Finite Bandwidth, I

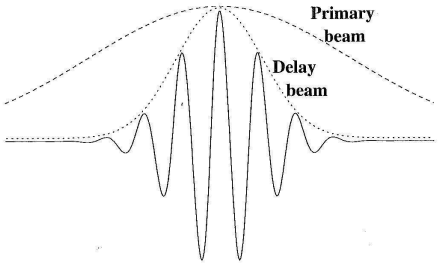

Burke & Graham-Smith (2002).

There are no natural monochromatic emitters in the sky. ⇒ Interferometer output is modified by the bandwidth of the receiving system.

Only for $\theta = 0$, constructive interference occurs at all wavelengths across the bandwidth. For increasing angles θ, the term $\cos(2\pi\, b_\lambda \theta)$ may be maximized at a center wavelength λ_0 but will decrease towards the wavelengths at the edges of the band pass. This diminishes the fringe amplitude and forms a delay beam, whose width is determined by the bandwidth. This is also called the Fringe-Washing Function.

The effect of the delay beam can be included in the expression for the effective area.

Effects of Finite Bandwidth, II

Assume a square band pass $g(\nu)$, unity over $\mathcal{B}$ around ν_0 and zero elsewhere:

$$g(\nu) = \Pi\left(\frac{\nu - \nu_0}{\mathcal{B}}\right) \tag{6.19}$$

The interferometer output is summed over all frequencies:

$$\begin{aligned}\langle S_{x,y}(\tau_g)\rangle &= \int_{\nu_0-\mathcal{B}/2}^{\nu_0+\mathcal{B}/2} A(\nu,\mathbf{s})\, S(\nu) \exp\left(-i2\pi\nu\tau_g\right) d\nu \\ &= A(\nu_0,\mathbf{s})\, S(\nu_0)\, \mathcal{B}\, \exp\left(-i2\pi\nu_0\tau_g\right) \mathrm{sinc}(\mathcal{B}\tau_g) \quad .\end{aligned}$$

When τ_g becomes equal to $1/\mathcal{B}$, the interferometer response is severely attenuated. The instrumental response τ_i compensates for this effect. The width of the delay beam is increased through: $\mathcal{B}\tau_g \rightarrow \mathcal{B}(\tau_g - \tau_i)$.

Effects of Finite Source Size, I

We did consider the modification of the correlator output due to emission at different frequencies within the bandpass. Now, we have to consider corrections due to emission arriving from different positions inside the primary beam, i.e., we go from point sources to brightness distribution.

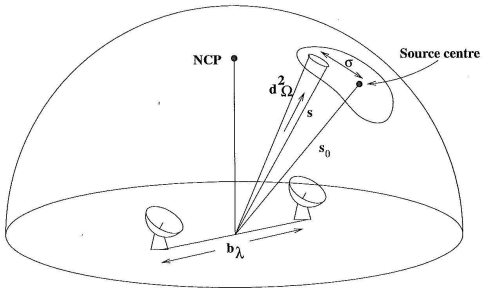

Burke & Graham-Smith (2002).

Radiation received from a small element $d^2\Omega$ of an extended radio source of brightness distribution $B_\nu(\mathbf{s})$. Reference direction $\mathbf{s}_0$ is chosen as the direction of maximum antenna gain and is called the phase tracking center. Vector in the plane of the sky from the phase tracking center to the source element is $\boldsymbol{\sigma}$.

Effects of Finite Source Size, II

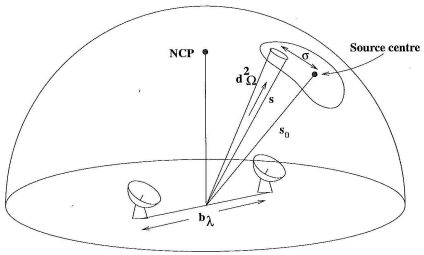

Burke & Graham-Smith (2002).

Interferometer response from element $d^2\Omega$:

$$S_{x,y}(\nu_0, \mathbf{s}_0 + \boldsymbol{\sigma}) = A(\mathbf{s}_0 + \boldsymbol{\sigma})\, B_\nu(\mathbf{s}_0 + \boldsymbol{\sigma})\, \mathcal{B}\, \exp\left[i2\pi\nu(\tau_g - \tau_i)\right] d^2\Omega \tag{6.20}$$

[with delay beam effects absorbed into $A(\mathrm{s}_0 + \sigma)$]. Integration over the entire source and band:

$$S_{x,y}(\mathbf{s}_0) = \mathcal{B} \int_{4\pi} A(\boldsymbol{\sigma})\, B_\nu(\boldsymbol{\sigma})\, \exp\left[i2\pi\nu(\tau_g - \tau_i)\right] d^2\Omega \tag{6.21}$$

Effects of Finite Source Size, III

Approximations:

- Small sources
- Flat source spectrum

  $\Rightarrow$ Delay-beam effects can be neglected. Use center frequency ν.
- Use relative antenna area $\mathcal{A}$, with value unity in direction $\mathbf{s}_0$.

Then, we get

$$S_{x,y}(\mathbf{s}_0) = \int \mathcal{A}(\boldsymbol{\sigma})\, B_\nu(\boldsymbol{\sigma})\, \exp\{i2\pi[\mathbf{b}_\lambda \cdot (\mathbf{s}_0 + \boldsymbol{\sigma}) - \nu\tau_\mathrm{i}]\}\, d^2\Omega \qquad (6.22)$$

Now consider an array of many antennas with baseline vectors $\mathbf{b}_{\mathrm{i,j}}$ from antenna i to antenna j. Choose an instrumental delay to cancel the tracking center delay. Define the *complex visibility* $V_{\mathrm{i,j}}$ as:

$$V_{\mathrm{i,j}} \equiv S_{x,y}(\mathbf{b}_{\mathrm{i,j}} \cdot \mathbf{s}_0 = \nu\tau_\mathrm{i}) = \int \mathcal{A}(\boldsymbol{\sigma})\, B_\nu(\boldsymbol{\sigma})\, \exp\left(i2\pi\mathbf{b}_{\mathrm{i,j},\lambda} \cdot \boldsymbol{\sigma}\right) d^2\Omega \quad . \qquad (6.23)$$

Effects of Finite Source Size, IV

Taking a deep breath and looking again at Eq. 6.23

$$V_{\mathrm{i,j}} = \int \mathcal{A}(\boldsymbol{\sigma})\, B_\nu(\boldsymbol{\sigma})\, \exp\left(i2\pi\mathbf{b}_{\mathrm{i,j},\lambda} \cdot \boldsymbol{\sigma}\right) d^2\Omega \qquad (6.23)$$

we see, what we achieved:

The complex visibility function $V_{\mathrm{i,j}}$ can be measured with multiple baselines $\mathbf{b}_{\mathrm{i,j}}$ in an array of radio telescopes, with an appropriate instrumental delay τ_i. The amplitude and phase of $V_{\mathrm{i,j}}$ are the principal observables in interferometry and are related to the brightness distribution on the sky $B_\nu(\boldsymbol{\sigma})$ via a Fourier-transform relationship.

We now need a coordinate system to measure the relative orientations of the antenna baselines in an array.

The u,v-plane, I

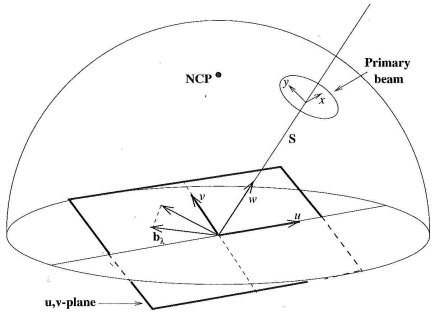

Burke & Graham-Smith (2002).

Define a right-handed rectilinear coordinate system (*u,v,w*), with the *w*-direction defined by $\mathbf{s}_0$. The *u,v*-plane is then orthogonal to $\mathbf{s}_0$ and contains $\boldsymbol{\sigma}$. After a small-angle approximation, this leads to (for details, see Burke & Graham-Smith, 2002):

$$V(u,v) \sim \int B(x,y)\, \exp\left[i2\pi(ux+vy)\right] dx\, dy \qquad (6.24)$$

or

$$V(u,v) \rightleftharpoons B(x,y) \qquad (6.25)$$

The u,v-plane, II

Summary, so far:

1. Build an array of N radio telescopes (that makes $N(N-1)/2$ baselines $\mathbf{b}_{\mathrm{i,j}}$)
2. Determine the relative positions of all antennas and express the coordinates of each baseline in the *u,v*-plane in units of wavelengths
3. Point all antennas to the source and record the receiver output
4. Feed the outputs into a correlator and form the cross-correlation
5. Find the instrumental delay τ_i that compensates for the phase-tracking delay
6. Measure the amplitude and phase of the correlator output for each baseline to form the complex visibility
7. Obtain the Fourier transform of the measured visibility function to get the brightness distribution on the sky

The next problem is how to do step 7. in practice.

Aperture Synthesis, I

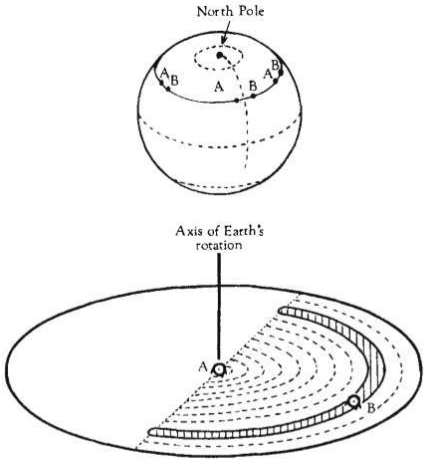

Ryle (1962)

Earth-Rotation Synthesis Mapping:

- Within 12 hours, an east-west baseline between two fixed antennas fills an elliptical closed track in the u,v-plane (circle for $\delta = 90°$).
- Changing the separation between both antennas allows to fill a continuous circular aperture in the u,v-plane
- At low declination, the tracks will have gaps
- Non east-west baselines have more complex tracks

Aperture Synthesis, II

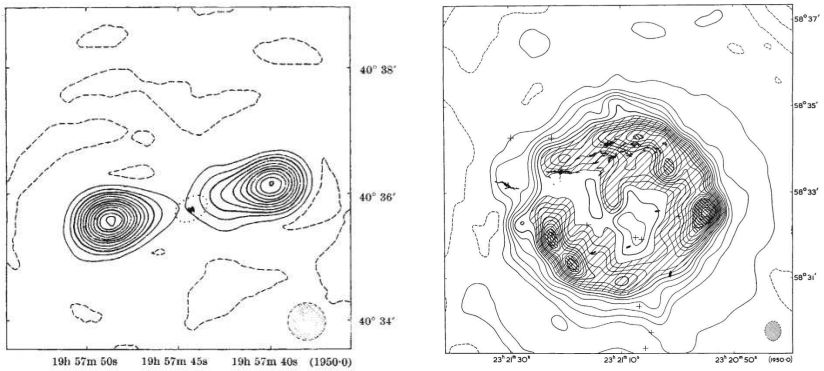

Two of the first earth-rotation-synthesis images, obtained by Ryle, Elsmore & Neville (1965) with the Cambridge One-Mile Telescope at 1.4 GHz: Cygnus A (left) and Cassiopeia A (right), the two brightest radio sources in the sky.

Aperture Synthesis, III

http://www.nrao.edu

The Very Large Array (VLA)

- First fringes: 1976
- 27 antennas in Y-shape, 25 m each
- Antennas move on tracks; four configurations:
  - A array: maximum separation 36 km
  - B-array – 10 km
  - C-array – 3.6 km
  - D-array – 1 km
- Currently in major upgrade → EVLA

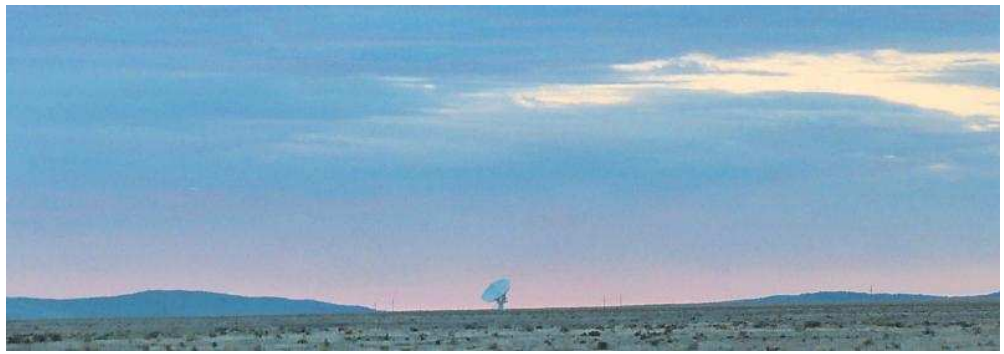

Lonely VLA antenna in A-configuration. Image: Bob Broilo, NRAO

Image: NRAO/AUI

Image: Bob Broilo, NRAO

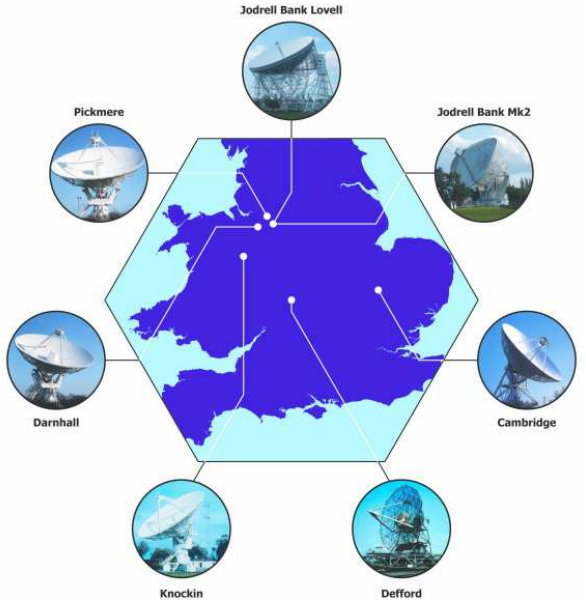

The *Multi-Element Radio Linked Interferometer Network* MERLIN
Image: `http://www.merlin.ac.uk`
Only 7 antennas (poor u,v-coverage) but better resolution than the VLA.

Aperture Synthesis, VI

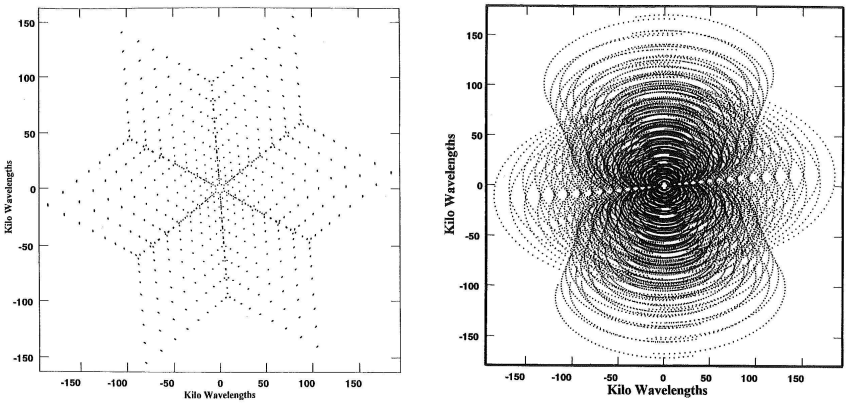

VLA u,v-coverage for a snapshot observation (left) and for an 8 hr tracking observation.

Images: Burke & Graham-Smith (2002)

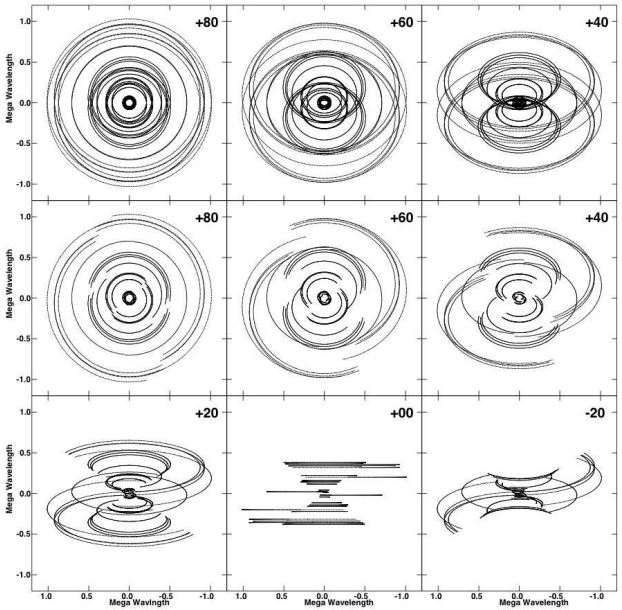

The MERLIN u,v-coverage (MERLIN User Guide: `http://www.merlin.ac.uk`)
Top: 24 h full tracks for circumpolar sources; middle: 12 h track for circumpolar sources; bottom: full tracks (< 12 h tracks for low-δ sources.

Obtaining Images, I

The basic relationship between the Visibility function and the brightness distribution is Eq. 6.24

$$V(u,v) = \int B(x,y)\, \exp\left[i2\pi(ux+vy)\right] dx\, dy$$

If $V(u,v)$ is known, the brightness distribution can be obtained by a simple Fourier inversion:

$$B(x,y) = \int V(u,v)\, \exp\left[-i2\pi(ux+vy)\right] du\, dv \quad . \tag{6.26}$$

In practice, we do not measure $V(u,v)$ continuously but a sampled visibility function $S(u,v)V(u,v)$, with

$$S(u,v) = \sum_{\mathsf{k}} \omega_{\mathsf{k}} \delta(u-u_{\mathsf{k}})\delta(v-v_{\mathsf{k}}) \quad . \tag{6.27}$$

Thus, we do not obtain the true brightness distribution but an inferior image, the so-called *dirty image*:

$$\begin{aligned} B^{\mathsf{D}}(x,y) &= \int S(u,v)\, V(u,v)\, \exp\left[-i2\pi(ux+vy)\right] du\, dv & (6.28)\\ &= \sum_{\mathsf{k}} V(u_{\mathsf{k}},v_{\mathsf{k}})\, \omega_{\mathsf{k}}\, \exp\left[-i2\pi(u_{\mathsf{k}}x+v_{\mathsf{k}}y)\right] & (6.29) \end{aligned}$$

Obtaining Images, II

The dirty image B^{D} is the Fourier transform of the sampled visibility function SV. From the *convolution theorem*, it follows that $B^{\mathsf{D}} = P^{\mathsf{D}} * B$.

The dirty image is the convolution of the true image with the *dirty beam* P^{D}.

P^{D} is equivalent to a point-spread function and is given by $P^{\mathsf{D}} = \mathcal{F}^{-1}(S)$:

$$P^{\mathsf{D}}(x,y) = \sum_{\mathsf{k}} \cos\left[2\pi(u_{\mathsf{k}}x+v_{\mathsf{k}}y)\right] \omega_{\mathsf{k}} \tag{6.30}$$

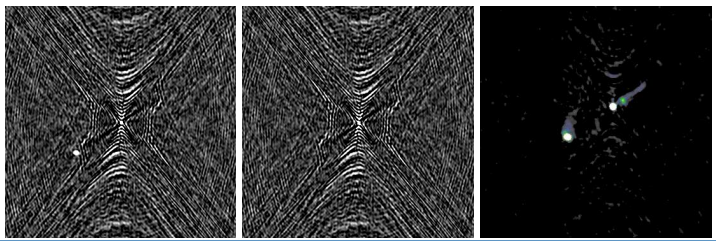

Dirty image, dirty beam and clean image of PKS 0521-365 from a VLA observation. Images: William C. Keel.

Obtaining Images, III

$$B^{\mathsf{D}}(x,y) = \sum_{\mathsf{k}} V(u_{\mathsf{k}},v_{\mathsf{k}})\, \omega_{\mathsf{k}}\, \exp\left[-i2\pi(u_{\mathsf{k}}x+v_{\mathsf{k}}y)\right]$$

The dirty image includes only structures sampled by the visibility function. Very large-scale structures correspond to very small spatial frequencies, which are usually not sampled at all.

A radio interferometer acts as a *spatial filter*!

Remember that the Fourier transform of a very wide Gaussian in the image domain is a very narrow Gaussian in the visibility domain. All telescopes in an array always have a minimum distance to each other. There is always a lack of *zero-baseline* information.

Similarly, an array with large gaps in the *u,v*-coverage may be insensitive to intermediate-scale structures.

Obtaining Images, IV

$$P^{\mathsf{D}}(x,y) = \sum_{\mathsf{k}} \cos\left[2\pi(u_{\mathsf{k}}x+v_{\mathsf{k}}y)\right] \omega_{\mathsf{k}}$$

The width of the central maximum in the dirty image in the x and y direction is approximately of the order of $1/u_{\mathsf{max}}$ and $1/v_{\mathsf{max}}$, respectively.
$\Rightarrow$ The maximum baselines determine the angular resolution.

Detailed shape of the dirty beam is determined by the weighting of the individual data points ω_{k}:

- *Natural weighting*: all data points get equal weight; this minimizes the noise in the image and maximizes the signal-to-noise ratio.
- *Uniform weighting*: gives less weight to densely-sampled regions of the *u,v*-plane; effectively, this weights up the long baselines resulting in a smaller beam but increased noise.

Obtaining Images, V

Sensitivity comes in two flavours:

- Baseline sensitivity: The source has to be detected on all individual baselines (i,j) within a coherence time (set by the atmosphere: tens of seconds to ~ 30 minutes depending on the frequency).
- Image sensitivity: Source-detection limit in the final image.

The *system equivalent flux density* (SEFD) expresses the system temperature in terms of the flux density of a source that delivers the same amount of power as the system itself. It can be shown (Walker, 1989) that the baseline sensitivity is

$$\Delta S_{\mathrm{i,j}} = \eta^{-1}\sqrt{\frac{\mathrm{SEFD_i}\cdot\mathrm{SEFD_j}}{2\Delta t\Delta\nu}} \tag{6.31}$$

where Δt is the integration time and $\Delta\nu$ is the bandwidth (η: efficiency factor).

Apart from electronics, the dominant quantity in SEFD is the effective collecting area A: SEFD $\propto A^{-1}$.

Obtaining Images, VI

Noise limit in the final image will be the combined sensitivity of all baselines integrated over the full time of the observation ($\gg$ coherence time).

$$\Delta S_{\mathrm{image}} = \eta^{-1}\mathrm{SEFD}^{*}/\sqrt{\frac{R}{2}T_{\mathrm{obs}}} \tag{6.32}$$

with

$$\mathrm{SEFD}^{*} = \frac{1}{\sqrt{\sum_{\mathrm{i,j}}\frac{1}{\mathrm{SEFD_i}\cdot\mathrm{SEFD_j}}}} \tag{6.33}$$

R is the data rate at which the signal is sampled.

Bottomline: Large dishes with low SEFD can ensure detections on all baselines, even to smaller antennas. They also dominate the image sensitivity.

Example (X-Band): $\mathrm{SEFD}_{\mathrm{Effelsberg,\,100\,m}} = 20$ Jy; $\mathrm{SEFD}_{\mathrm{TIGO,6\,m}} = 9000$ Jy; $\Delta S_{\mathrm{Effbg,TIGO}}(10\,\mathrm{min}) = 2.2$ mJy. In any realistic VLBI array, TIGO would only incrementally improve the image sensitivity, but because of its remore location (Chile) it may substantially improve angular resolution.

Calibration of Interferometer Data

Two classes of calibration sources are needed for all interferometer experiments:

- Flux calibrators are sources with accurately known fluxes that vary at worst slowly with time. They need to be compact, so that they are not resolved by the long baselines. Problem: small sources tend to be variable.
- Phase calibrators may vary, but they need to be stable in position and close to the target source.

The typical interferometric observation includes scans on the target source, frequent scans on phase calibrators and at least a few scans on a flux calibrator.

VLBI, I

VLBI: Very Long Baseline Interferometry

Main differences to connected interferometers are

- No direct connection to the correlator (except for e-VLBI)
  $\Rightarrow$ Data have to be recorded and shipped to the correlator
- Baselines about 2 orders of magnitude larger
  $\Rightarrow$ Angular resolution is about 2 orders of magnitude better
- Antenna locations are arbitrary; large gaps in the *u,v*-plane
  $\Rightarrow$ Image reconstruction is more tricky

VLBI, II

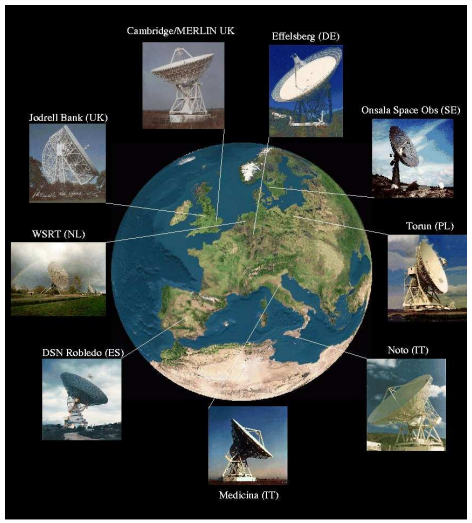

The European VLBI Network (EVN) is an array of 18 individual antennas

- Consortium of major radio astronomical institutes in Europe
- Coordinated observations only during 3 sessions per year (plus intermittent e-VLBI sessions)
- Telescopes have been built *for other purposes* but team-up for EVN observations
- Includes large dishes like Effelsberg, yielding a sensitivity of $\mu\,Jy$
- Inclusion of telescopes in China increases the angular resolution up to ~ 0.15 mas

`http://www.evlbi.org`

VLBI, III

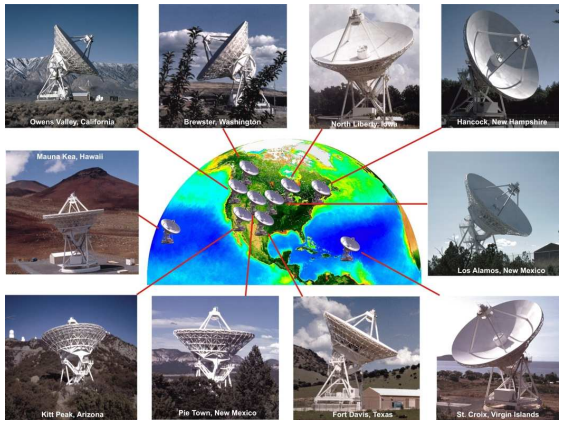

The Very Long Baseline Array (VLBA):

- Only dedicated VLBI array
- 10 identical 25 m telescopes
- Longest baseline between St. Croix (Virgin Islands) to Mauna Kea (Hawaii) is 8611 km
- Maximum angular resolution is 0.17 mas at 7 mm

`http://www.nrao.edu`

VLBI, IV

Other VLBI Networks:

- HSA: High Sensitivity Array – consists of Effelsberg, Arecibo, GBT, VLA, VLBA
- LBA: Long Baseline Array – Southern Hemisphere VLBI array
- GMVA: Global Millimtre VLBI Array – 3 mm VLBI
- IVS: International VLBI Service – mostly geodetic and astrometric research
- KVN and VERA: Korean and Japanese arrays; plans to team up as East Asian VLBI Array (EAVN)

VLBI, V

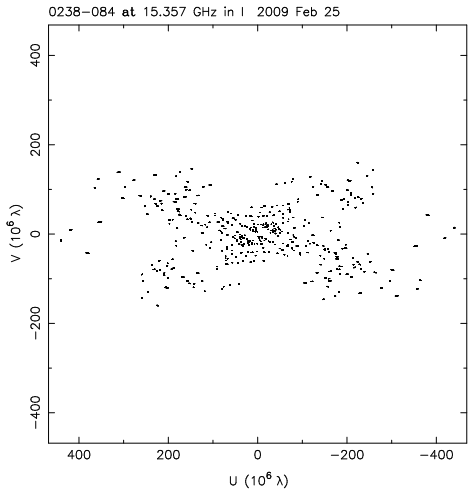

A typical u,v-coverage for a survey VLBA observation.

VLBI, VI

Data are recorded at the individual stations. Relative phases of the signals are unknown. Even worse: large differences in the transmission paths through the atmosphere and ionosphere. In sum, a baseline (i,j) is not measuring

$$|V_{i,j}| \exp i\Phi_{0,i,j}$$

but

$$|V_{i,j}| \exp i(\Phi_{0,i,j} + \Delta\Phi_{i,j}) \quad .$$

The relative phases of the recorded signals have to be determined after the actual observation: fringe finding (VLBI correlator) and self calibration (astronomer during data analysis).

Fortunately, there is a *phase closure relationship* for every triangle (i,j,k) of antennas, which is independent of the errors introduced by the atmosphere and ionosphere.

VLBI, VII

The phase of the observed visibility on baseline (i,j) is

$$\Phi_{i,j} = \Phi_{0,i,j} + \Delta\Phi_{i,j} = \Phi_{0,i,j} + (\Theta_i - \Theta_j) \tag{6.34}$$

with $\Theta_{i,j}$ being the phase error introduced at station (i,j).

The *closure phase* in a triangle of three telescopes (i,j,k) is

$$\begin{aligned} c_{i,j,k} &= \Phi_{0,i,j} + \Phi_{0,j,k} + \Phi_{0,k,i} + \Theta_i - \Theta_j + \Theta_j - \Theta_k + \Theta_k - \Theta_i & (6.35)\\ &= \Phi_{0,i,j} + \Phi_{0,j,k} + \Phi_{0,k,i} & (6.36) \end{aligned}$$

In the image reconstruction, the phases $\Phi_{i,j}$ are self-calibrated, preserving the closure phases $c_{i,j,k}$.

After applying phase self-calibration, there is no way to tell if one corrected for one single phase error at only one station or for multiple errors at multiple stations. Effectively, this waives all information about the absolute source position!

VLBI, VIII

There is also a closure relationship that allows one to compensate for amplitude errors.

On the baseline (i,j), the measured fringe visibility amplitude $|V_{i,j}|$ is affected by gain errors at the stations

$$|V_{i,j}| = g_i g_j |V_{0,i,j}| \tag{6.37}$$

The *closure amplitude* in a set of four antennas (i,j,k,l) is

$$a_{i,j,k,l} = \frac{|V_{i,j}||V_{k,l}|}{|V_{j,k}||V_{l,i}|} = \frac{g_i g_j |V_{0,i,j}| g_k g_l |V_{0,k,l}|}{g_j g_k |V_{0,j,k}| g_l g_i |V_{0,l,i}|} = \frac{|V_{0,i,j}||V_{0,k,l}|}{|V_{0,j,k}||V_{0,l,i}|} \tag{6.38}$$

Amplitude self-calibration is a dicey issue: very extended structures, seen on only the longest baselines can easily be misinterpreted as an amplitude error!

Both closure relationships are most effectively used in large arrays, recovering fractions of $(N-2)/N$ and $(N-3)/(N-1)$ of the original $N(N-1)/2$ visibility amplitudes and phases, respectively.

Summary of Interferometer Theory

An interferometer measures the complex visibility

$$V(u,v) = \int B(x,y) \exp\left[i2\pi(ux+vy)\right] dx\, dy \tag{6.24}$$

Problem: $V(u,v)$ is a continuous function that is only measured at $N(N-1)/2$ points with an N-element interferometer, i.e., we really measure:

$$V(u,v)S(u,v) = V(u,v) \sum_k \omega_k \delta(u-u_k)\delta(v-v_k) \quad . \tag{6.27}$$

Fourier inversion of this sampled visibility function $S(u,v)V(u,v)$ yields the dirty image:

$$B^D(x,y) = \sum_k V(u_k,v_k)\, \omega_k \exp\left[-i2\pi(u_k x + v_k y)\right] \tag{6.29}$$

which is the true image convolved with the dirty beam (PSF).

Image deconvolution (e.g., using hybrid mapping) recovers the CLEAN image.

Demo: Virtual Radio Interferometer, I

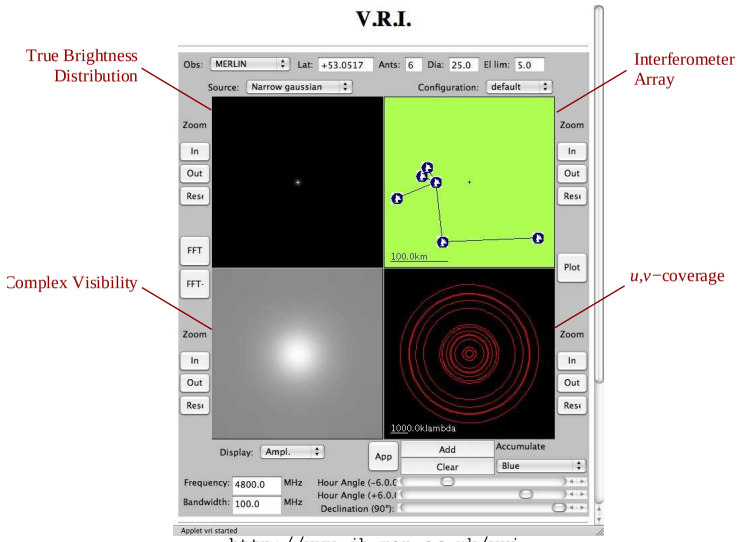

http://www.jb.man.ac.uk/vri

Demo: Virtual Radio Interferometer, II

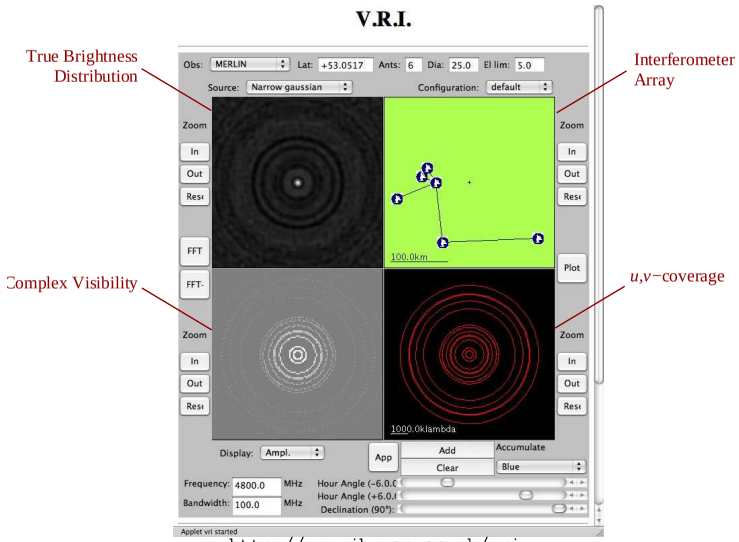

http://www.jb.man.ac.uk/vri

Hybrid Imaging, I

The final step of interferometric data analysis is the Fourier inversion of the precalibrated visibilities measured at various positions in the u,v-plane and the deconvolution of the dirty image.

Most common procedure: the *CLEAN algorithm* (Högbom, 1974):

1. Interpolate available u,v-data points to lie on a regular grid.
2. Perform a Fast Fourier transform of the gridded data to obtain a dirty image.
3. Identify the brightest pixel in the dirty image and subtract the dirty-beam response of a point source (including side lobes) of a small fraction of the dirty-map peak signal (*loop gain*: typically 0.02 to 0.05).
4. Store this first model (the point source) in a temporary map.
5. Repeat steps 3 and 4 on the new maxima of the dirty image (now called the *residual map*). This iteratively decreases the amplitudes in the residual map – the image is *cleaned*.
6. Stop when the residual map does no longer exhibit clear localized maxima.
7. Convolve the developed *clean* model with a synthesized Gaussian beam –the *clean beam*– whose FWHM equals the width of the main lobe of the dirty beam. This yields a *clean image*.
8. Add the residual map to the clean image.

Hybrid Imaging, II

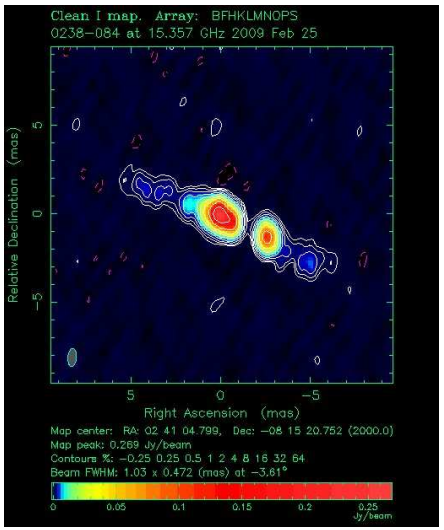

Demo: DIFMAP `ftp://ftp.astro.caltech.edu/pub/difmap/difmap.html`

Hybrid Imaging, III

A modification of the *CLEAN algorithm* is the so-called *hybrid imaging*, which makes use of the closure relationships of the visibility phases and amplitudes. This technique is widely used, particularly in VLBI imaging, where the original phases and amplitudes can be affected by substantial errors.

The general modifications are:

- After obtaining a first model that reproduces the *u,v*-data reasonably well, a phase selfcalibration is applied. The now improved data are used to obtain a second model.
- The clean-selfcal process is repeated until no further improvement of the model is possible. This model is then used to apply an amplitude self-calibration. For this initial amplitude self calibration, a long solution interval is used to correct only for constant or slowly varying errors in the visibility amplitudes.
- A new cycle begins: the previous model is waived and the phase- and amplitude-calibrated data are used to develop a new model with clean-selfcal iterations. The best obtainable model is used for a new amplitude self calibration, now with a smaller solution interval.
- This iterative process is reapeated with smaller and smaller solution intervals until finally a self-consistent model is obtained that reproduces the calibrated data.

Hybrid Imaging, IV

It has to be noted that the process of hybrid mapping is not unique. Subtle differences in the final map are expected if different hybrid maps are produced from the same data. However, these differences should all be on a $(< 3 - 5\,\sigma)$ level, i.e., they should be visible only in the lower two contour lines of the final image.

Never trust the lowest contour lines in VLBI maps!

Hybrid Imaging, V

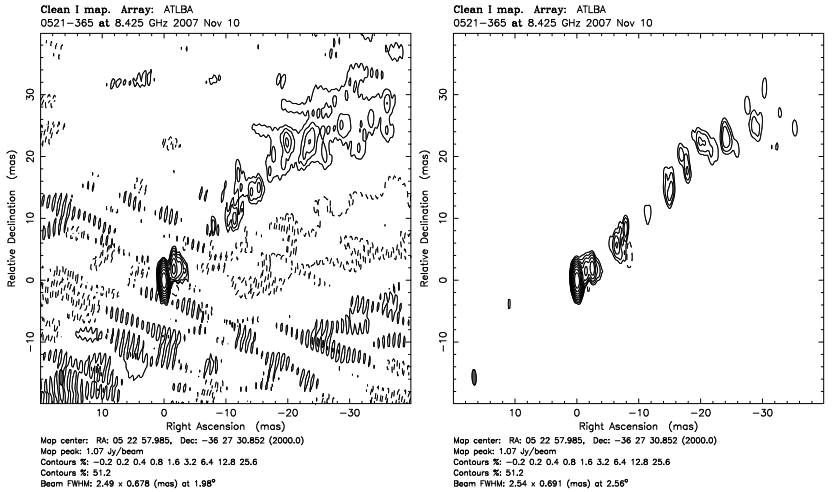

VLBI image of the BL Lac object PKS 0521-365 obtained with the LBA as part of the TANAMI program.

Left: with only phase self calibration; Right: with phase and amplitude self calibration.

Burke, B. F., & Graham-Smith, F., 2002, An Introduction to Radio Astronomy: Second Edition

Högbom, J. A., 1974, A&AS, 15, 417

Ryle, M., 1962, Nature, 194, 517

Ryle, M., Elsmore, B., & Neville, A. C., 1965, Nature, 205, 1259

Walker, R. C., 1989, in Techniques and Applications of Very Long Baseline Interferometry, 163

The Quest for Angular Resolution

Remember again: Angular resolution of

– a single radio dish (e.g., Effelsberg): $\theta \sim 0.42'$ $\left(\frac{\lambda}{[1\,\mathrm{cm}]}/\frac{D}{[100\,\mathrm{m}]}\right)$

– a connected interferometer (e.g., VLA): $\theta \sim 0.07''$ $\left(\frac{\lambda}{[1\,\mathrm{cm}]}/\frac{D}{[36\,\mathrm{km}]}\right)$

– VLBI (e.g., the VLBA): $\theta \sim 0.0003''$ $\left(\frac{\lambda}{[1\,\mathrm{cm}]}/\frac{D}{[8611\,\mathrm{km}]}\right)$

The VLBA already extends to $\sim$ 65 % of the earth diamter. Further increase of earth-bound baselines yields only small improvements in angular resolution. The microarcsecond regime can be reached by:

- Going to space:
  - VSOP [1997-2005, `http://www.vsop.isas.jaxa.jp`]
  - VSOP-2 [2012+, `http://www.vsop.isas.jaxa.jp/vsop2`]
  - Radioastron [2009+, `http://www.asc.rssi.ru/radioastron`]
- Going to millimetre wavelengths:
  - GMVA [`http://www.mpifr-bonn.mpg.de/div/vlbi/globalmm`]

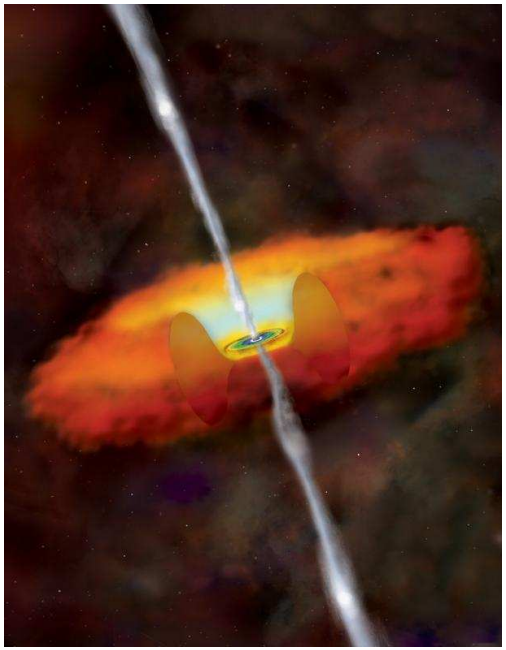

The AGN standard model. Image: CXC/Weiss

The Quest for Angular Resolution

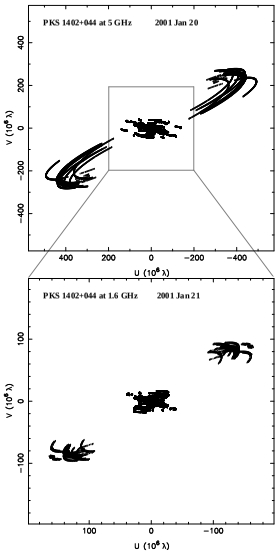

Images: Yang et al. (2008), `http://www.vsop.isas.jaxa.jp`

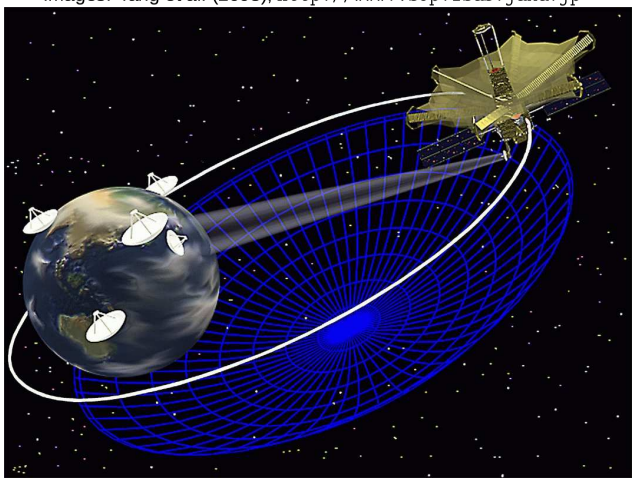

Radio Loud AGN – Context, II

Radio-loud AGN are an important sub-class of active galactic nuclei.

Question: What makes an AGN radio-loud?
Answer: Jets!

Jets emit across the whole electromagnetic spectrum and are classical targets of multiwavelength astronomy. They consist of highly relativistic outflows, which are bright sources of radio, optical, X-ray, and γ-ray emission.

VLBI provides the only method to image the most compact multiwavelength-emission regions at the base of the jets. Relativistic bulk motions can be directly measured and feed into broadband emission models.

VLA Images of Radio Galaxies, I

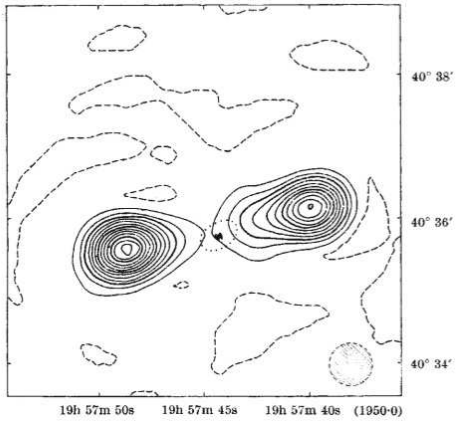

Cygnus A with the Cambridge One-Mile Telescope at 1.4 GHz (Ryle, Elsmore & Neville, 1965).

VLA Images of Radio Galaxies, II

The powerful radio galaxy Cygnus A at $z = 0.057$ ($d = 230$ Mpc).

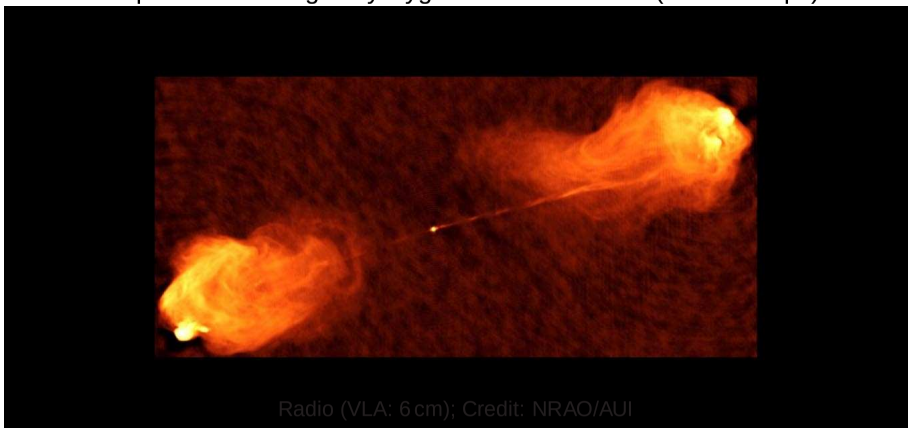

Size: $\sim$ 2.2 arcmin $\sim$ 600000 ly, about eight times the size of the milky way!

Radio morphology: Core – Jets – Hotspots – Lobes

VLA Images of Radio Galaxies, III

The powerful radio galaxy Cygnus A at $z = 0.057$ ($d = 230$ Mpc).

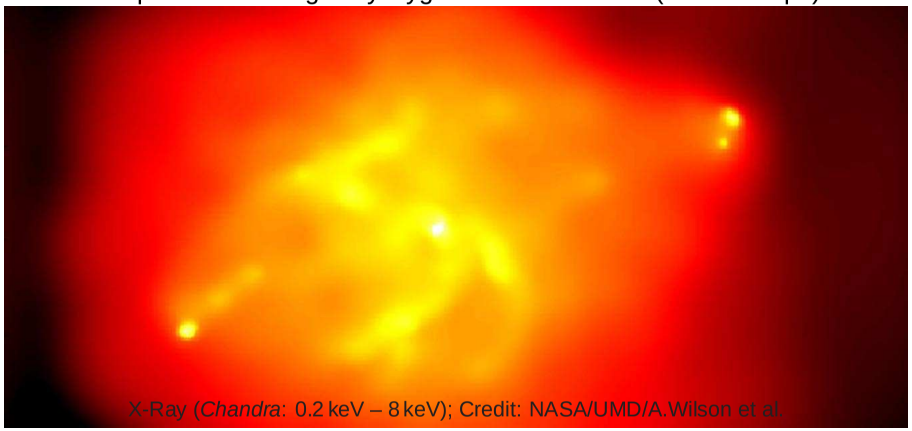

Size: $\sim$ 2.2 arcmin $\sim$ 600000 ly, about eight times the size of the milky way!

Radio morphology: Core – Jets – Hotspots – Lobes

X-Ray morphology: Nucleus – Cavity – Hotspots

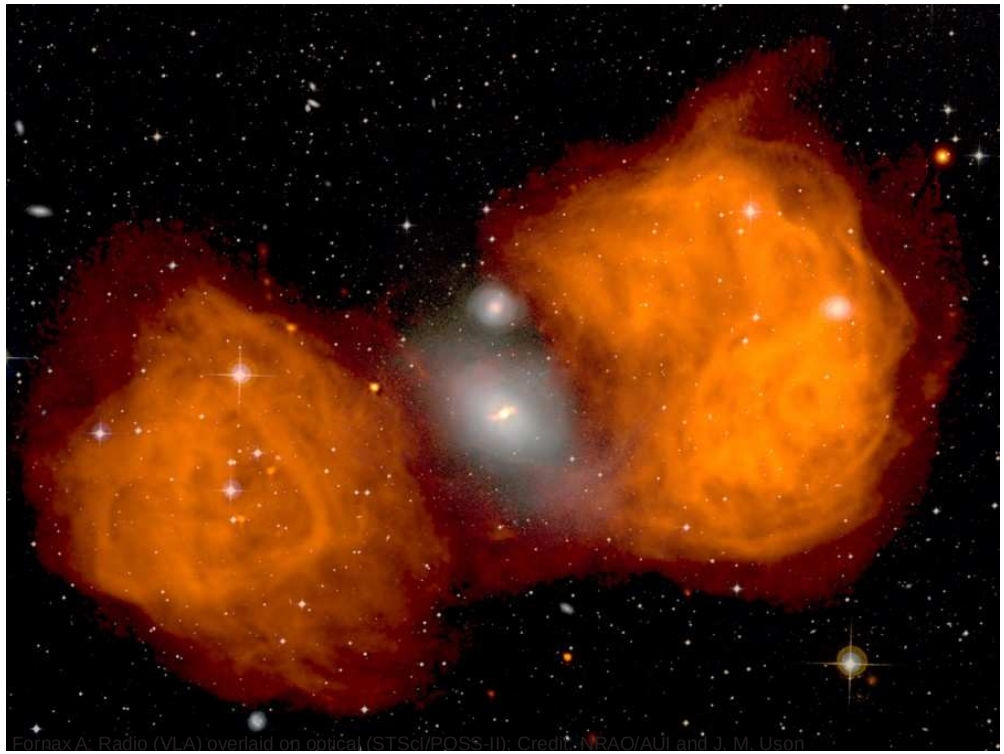

Classification of Radio-Loud AGN, I

Classification based on morphology and radio spectrum:

1. Powerful double-lobed radio galaxies with hotspots and a steep radio spectrum falling toward higher frequencies (Fanaroff-Riley class II, FR II)
2. Weaker steep-spectrum, double-lobed radio galaxies without leading hotspots (FR I types)
3. Core-dominated flat-spectrum sources (Blazars: quasars and BL Lac objects)
4. Compact steep-spectrum sources (CSS sources) and gigahertz-peaked spectrum sources (GPS sources); no large-scale radio structure; morphological classification term: compact symmetric objects (CSOs) or compact doubles

Observing technique and frequency strongly affects sample composition (e.g., low-frequency flux-density limited surveys tend to select steep-spectrum sources. Flat-spectrum sources are classical targets for Very-Long-Baseline Interferometry (VLBI) observations, which are sensitive to compact emission.

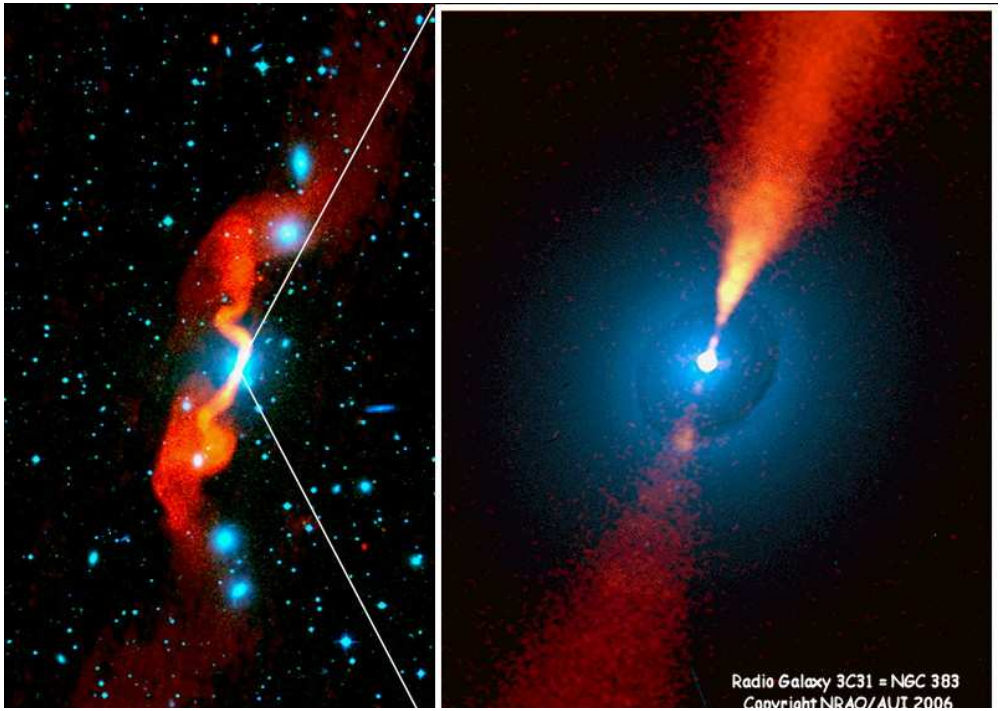

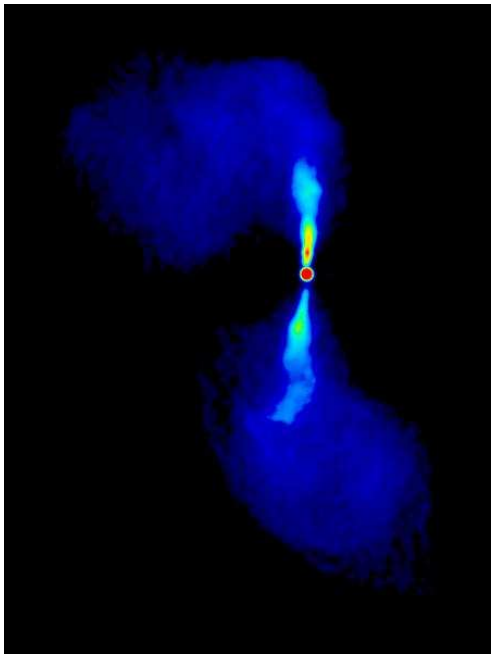

Fanaroff-Riley Type 1: asymmetric jets with wide opening angle ending in plumes

M84 (3C272.1) (Laing & Bridle, 1987):
VLA 4885 MHz, 134″ × 170″; see also
`www.jb.man.ac.uk/atlas/other/3C272P1.html`

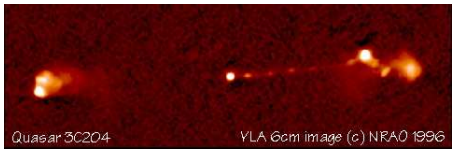

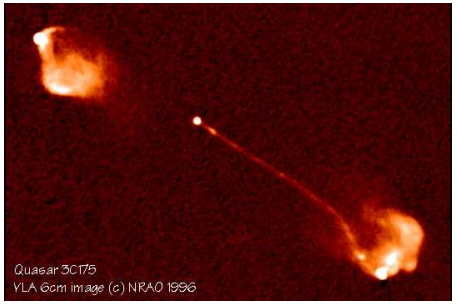

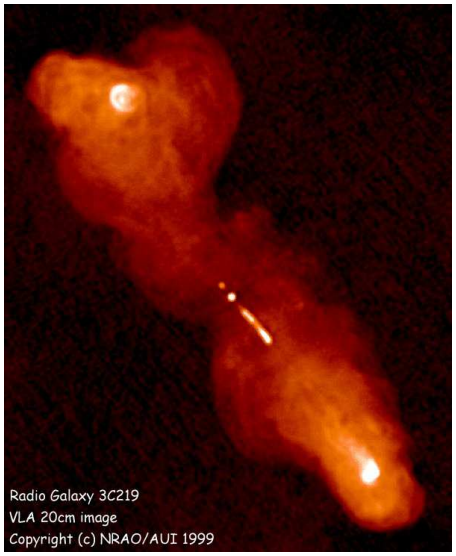

A. Bridle, `www.cv.nrao.edu/~abridle/images.htm`

Fanaroff-Riley Type 2: powerful lobe dominated doubles; jets often one-sided

Radio Interferometry: Longer baselines and higher frequencies yield higher resolution

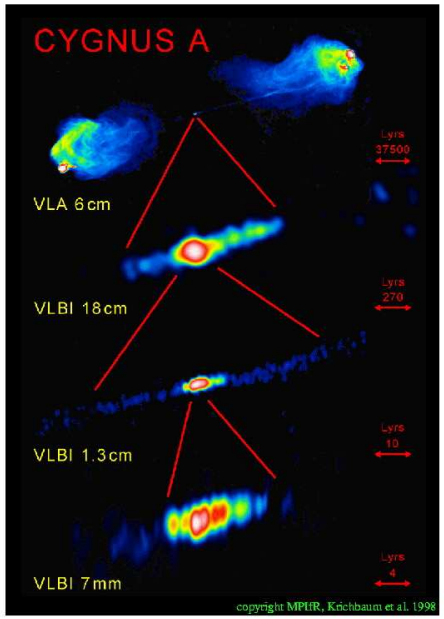

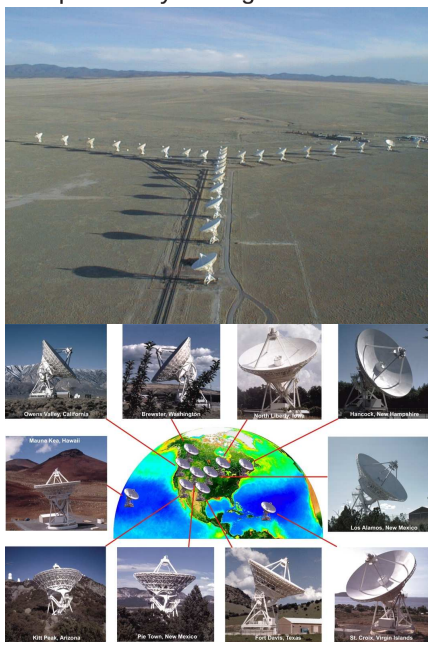

Image courtesy of MPIfR, NRAO/AUI and Earth image courtesy of the SeaWiFS Project NASA/GSFC and ORBIMAGE

Flat-Spectrum Radio Sources: Blazars

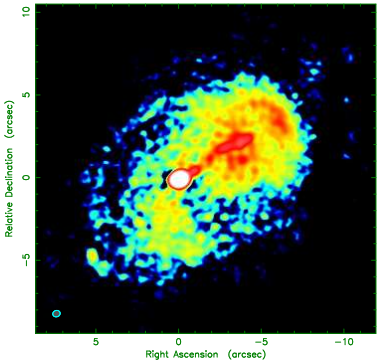

Image courtesy: U. Bach, MPIfR

0716+714, BL Lac object at redshift $z = 0.3$ (Nilsson et al., 2008)

Highly variable, core dominated object

"Fried-egg" morphology – really the end-on view of a radio lobe?

Almost all the flux density is concentrated within a few milliarcseconds-size compact jet!

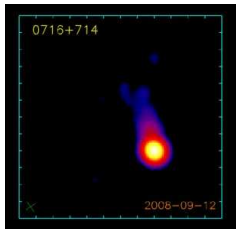

Image Courtesy: MOJAVE

"Roughly equal numbers of steep-spectrum extended double-lobed sources and flat-spectrum objects that are unresolved on arcsec scales."

(Zensus, 1997)

Radio Spectra, I

Jets are observed to have strong polarization and power law radio spectrum. These are characteristics of synchrotron radiation.

Synchrotron-Radiation (=Magnetobremsstrahlung): Radiation emitted by relativistic electrons in a magnetic field.

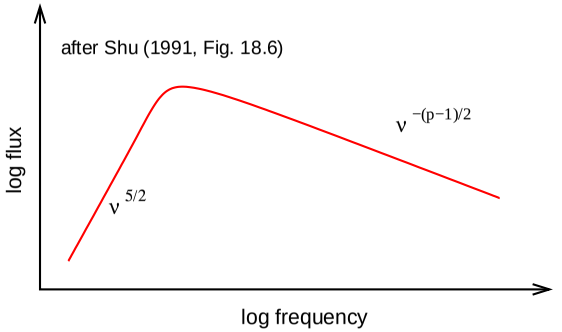

Spectrum of a single synchrotron-emitting blob:
At low ν: optically thick.
At high ν: optically thin.

Turnover: $\tau = 1$ surface

$\tau \propto R$ and $\nu(\tau = 1) \propto R^{-1}$

(R: size of the emitting region).

Radio Spectra, II

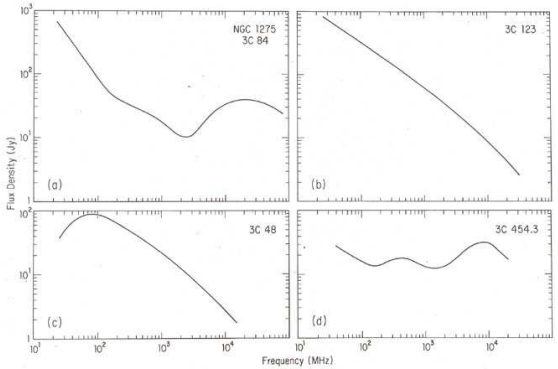

- NGC 1275: extended steep-spectrum emission plus compact self-absorbed nucleus
- 3C123: 3C 123: optically thin at all plotted frequencies
- 3C 48: self-absorbed below 100 MHz
- 3C454.3: superposition of many jet regions which become opaque at different frequencies (flat-spectrum radio quasar)

Multifrequency VLBI Observations, I

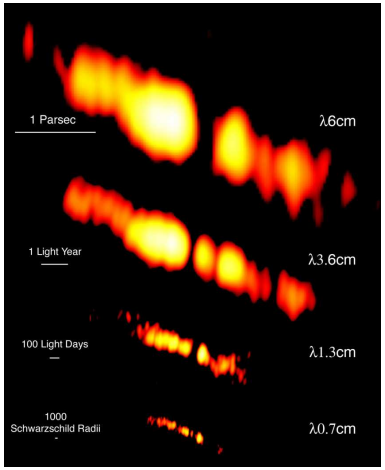

The Twin-Jet in NGC 1052 observed with the VLBA at 4 frequencies; Image: M. Kadler

At higher frequencies

1. the angular resolution improves
2. the structure changes: different parts of the jet dominate the emission at different frequencies (superposition to a flat spectrum)
3. emission shows up in the central emission gap; spectral index $\alpha > 2.5 \Rightarrow$ no self absorption
4. the absorption is caused by free-free absorption in the circumnuclear torus; at high frequencies, the torus becomes transparent

Kameno et al. (2001); Kadler et al. (2004)

Multifrequency VLBI Observations, II

Movie: Spinning the dial on NGC 1052

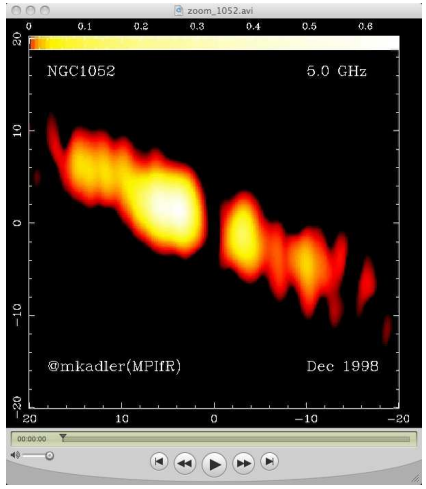

http://www.sternwarte.uni-erlangen.de/~kadler/movies/zoom_1052.avi

Apparent Superluminal Motion, I

VLBI resolution 1 mas

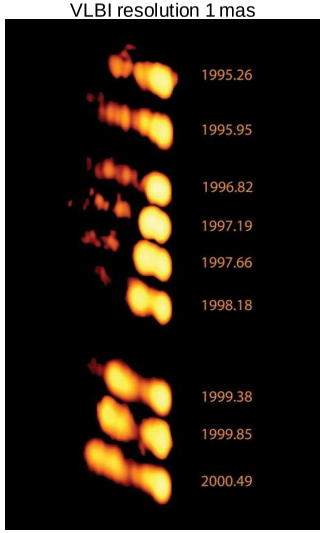

Kadler et al. (2008)

3C 111: Apparent speed of jet: $\sim 5c$

Superluminal motion: The apparent velocities of jet features ("blobs") measured in many AGN jets often exceed the speed of light.

First discovered in 1971 in 3C279
(Cohen et al., 1971; Whitney et al., 1971).

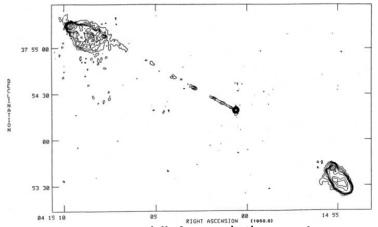

VLA resolution ~ 1 arcsec

Apparent Superluminal Motion, II

Movies: Examples of superluminal motion in AGN jets

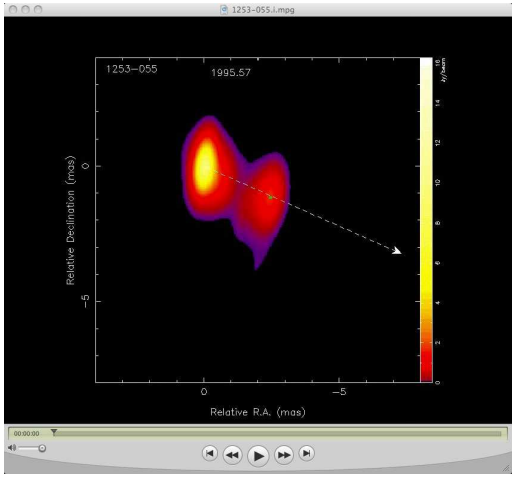

http://www.physics.purdue.edu/astro/MOJAVE/movies.html

Superluminal Motion Demo:

www.physics.purdue.edu/MOJAVE/superluminal.swf

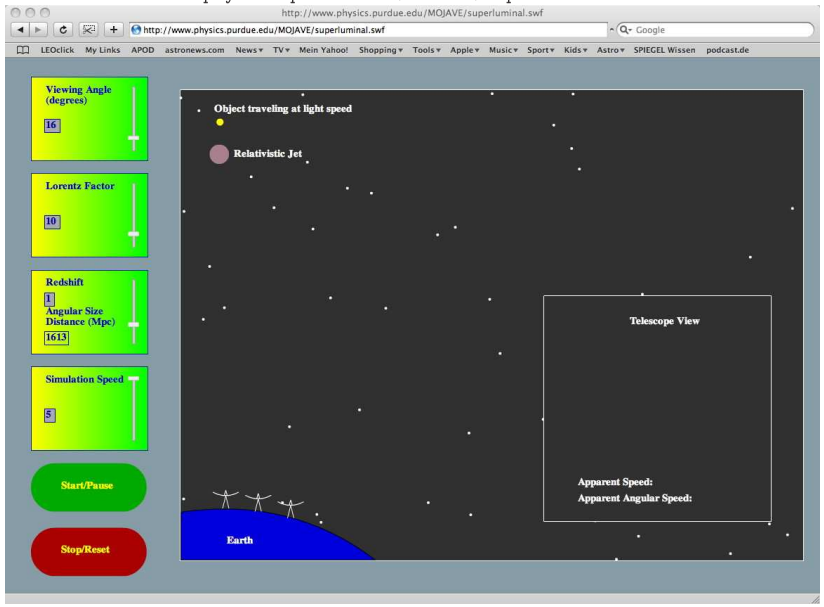

$t_1 = 0$: Blob is ejected from core and emits first photon.

Superluminal Motion Demo:

www.physics.purdue.edu/MOJAVE/superluminal.swf

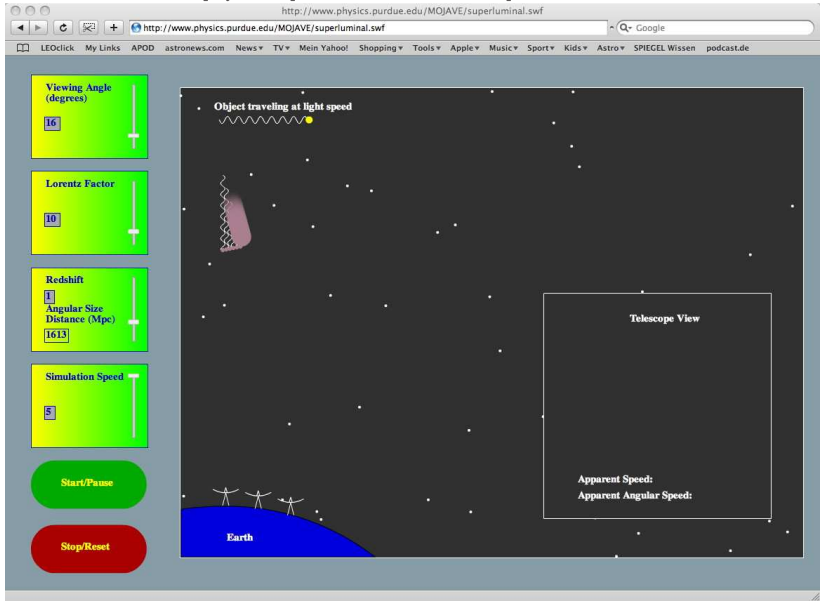

t_2: First photons and blob travel towards earth.

Superluminal Motion Demo:

www.physics.purdue.edu/MOJAVE/superluminal.swf

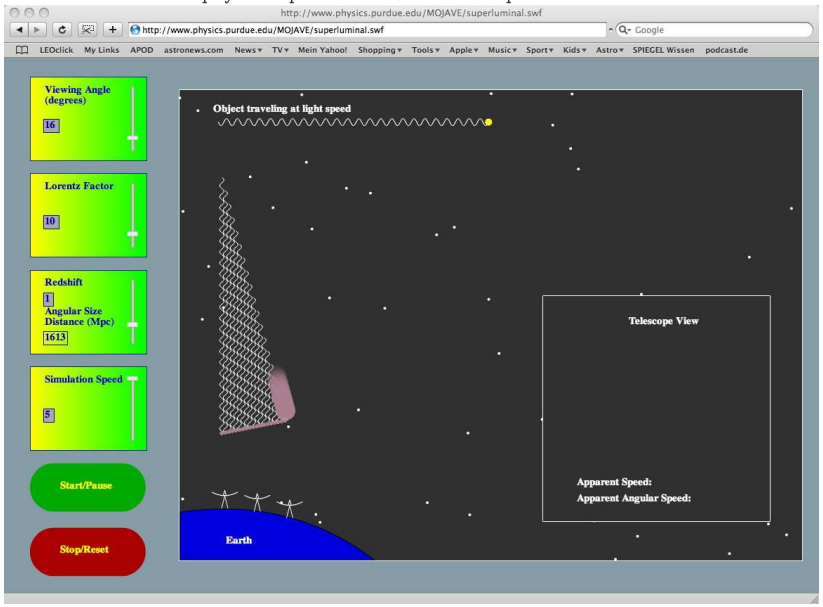

t_3: Blob almost keeps the pace of the photons.

Superluminal Motion Demo:

www.physics.purdue.edu/MOJAVE/superluminal.swf

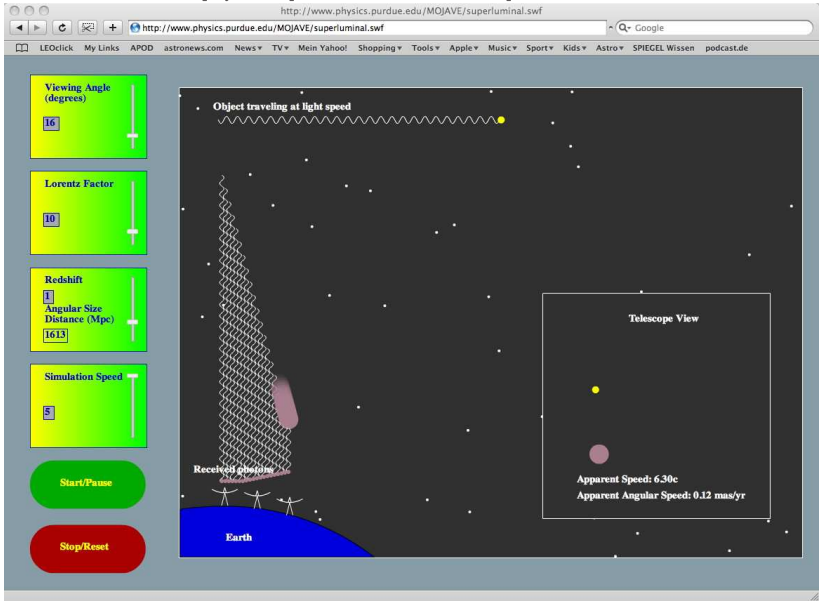

t_4: First photons arrive at telescope. Observer starts to take the time.

Superluminal Motion Demo:

www.physics.purdue.edu/MOJAVE/superluminal.swf

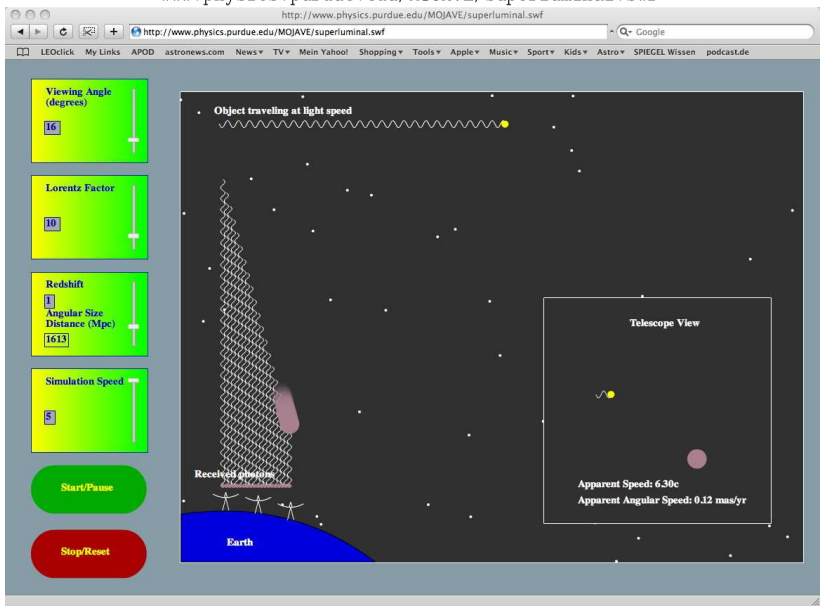

t_5: The last photons have a much smaller way to travel and come in quickly.

Observer measures superluminal motion on the sky!

Apparent Superluminal Motion, VIII

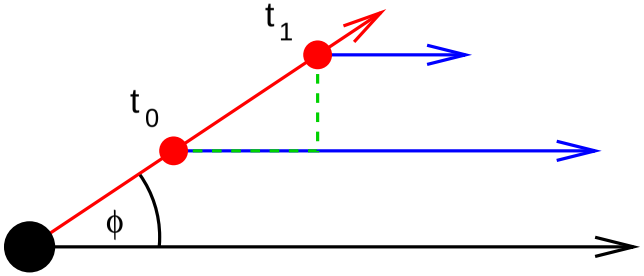

Consider blob moving towards us with speed v and angle ϕ with respect to line of sight, emitting light signals at t_0 and $t_1 = t_0 + \Delta t_e$

Light travel time: Observer sees signals separated by

$$\Delta t_o = \Delta t_e - \Delta t_e \frac{v}{c} \cos\phi = \left(1 - \frac{v}{c}\cos\phi\right) \Delta t_e \qquad (6.39)$$

Observed distance traveled in plane of sky:

$$\Delta \ell_\perp = v \Delta t_e \sin\phi \qquad (6.40)$$

Apparent Superluminal Motion, IX

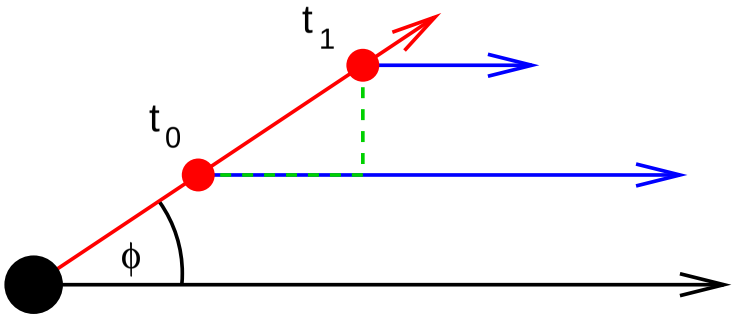

Apparent velocity deduced from observations:

$$v_{app} = \frac{\Delta \ell_\perp}{\Delta t_o} = \frac{v \Delta t_e \sin\phi}{\left(1 - \frac{v}{c}\cos\phi\right) \Delta t_e} = \frac{v \sin\phi}{\left(1 - \frac{v}{c}\cos\phi\right)} \qquad (6.41)$$

$\Longrightarrow$ For v/c large and ϕ small: $v_{app} > c$

Apparent Superluminal Motion, X

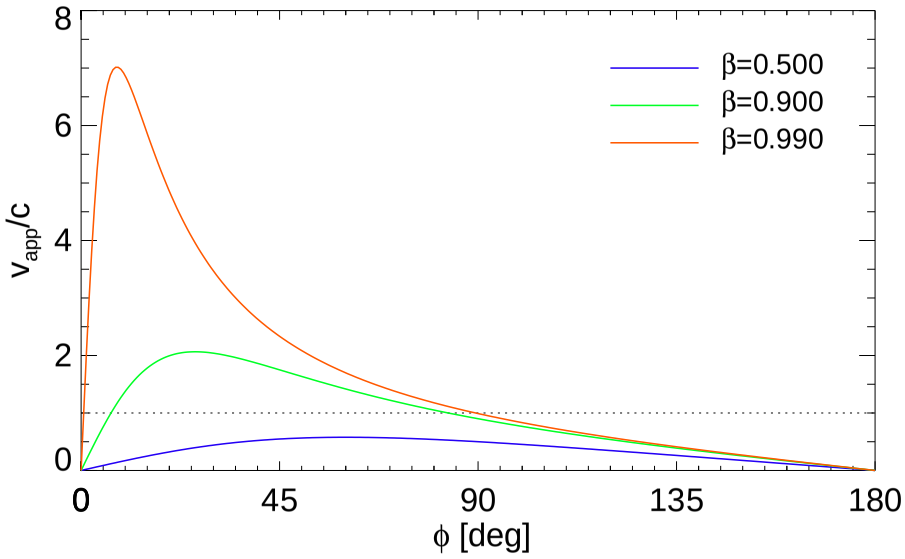

Relativistic Boosting, I

If jet plasma is moving at relativistic speeds, we have to consider also other relativistic effects.

Remember that

$$\nu = \frac{1}{\Delta t_{\rm A}} = \frac{\nu'}{\gamma\left(1 - \frac{v}{c}\cos\theta\right)} \tag{6.42}$$

and

$$\gamma = \frac{1}{\sqrt{1 - \frac{v^2}{c^2}}} \quad . \tag{6.43}$$

This defines the relativistic Doppler factor

$$\mathcal{D} = \frac{1}{\gamma\left(1 - \frac{v}{c}\cos\theta\right)} = \frac{\sqrt{1-\beta^2}}{1 - \beta\cos\theta} \tag{6.44}$$

(the difference to the classical Doppler factor is only the γ factor).

The Doppler factor is a strong function of the aspect angle and can become very large for $v \to c$.

Relativistic Boosting, II

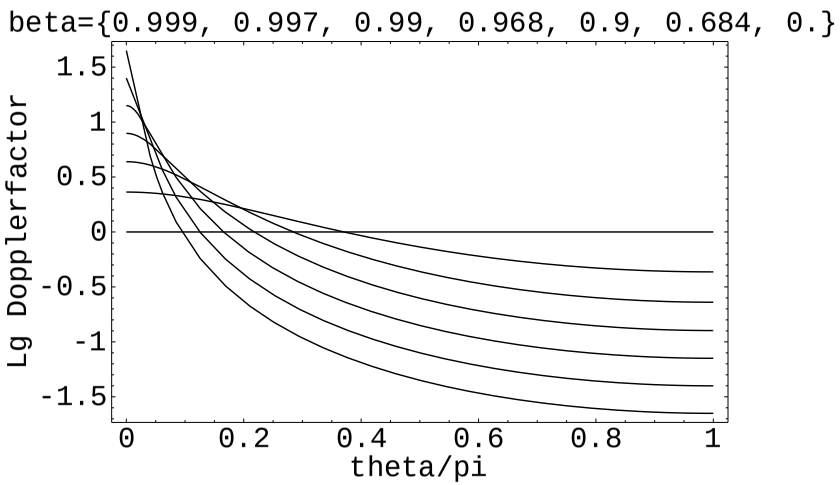

Within $\sim 1 - 2$ deg, the Doppler factor can approach values of 100 or higher.

Relativistic Boosting, III

One can show (i.e., Rybicki & Lightman, chap. 4.9) that S_ν/ν^3 is invariant under Lorentz transformation, where S_ν is the flux density.

Therefore, observed intensity of a moving blob:

$$\frac{S(\nu_{\rm obs})}{\nu_{\rm obs}^3} = \frac{S(\nu_{\rm em})}{\nu_{\rm em}^3} \tag{6.45}$$

and

$$S(\nu_{\rm obs}) = \nu_{\rm obs}^3 \frac{S(\nu_{\rm em})}{\nu_{\rm em}^3} = \mathcal{D}^3 S(\nu_{\rm em}) \tag{6.46}$$

Specifically, for a blob with a power law spectrum ($S(\nu) = A\nu^\alpha$):

$$S(\nu_{\rm obs}) = \mathcal{D}^3 A \nu_{\rm em}^\alpha = \mathcal{D}^3 A \mathcal{D}^{-\alpha} \nu_{\rm obs}^\alpha \tag{6.47}$$

$$S(\nu_{\rm obs}) = \mathcal{D}^{3-\alpha} S(\nu_{\rm em}) \quad . \tag{6.48}$$

Even for relatively modest relativistic velocities of $0.97c$ ($\gamma \simeq 4$), for example, the flux in the forward direction can be boosted by a factor 1000, while it is reduced by a factor 1000 in the backward direction!

Jet One-Sidedness, I

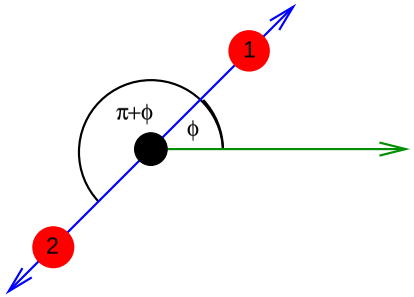

Now take a source emitting blobs symmetrically in two directions.

From Eq. (6.47) the ratio of fluxes from the blobs is

$$\frac{S_1}{S_2} = \left(\frac{1 + \beta\cos\phi}{1 - \beta\cos\phi}\right)^{3-\alpha} \tag{6.49}$$

Even for mildly relativistic speeds and large angles, features on the approaching side are always significantly brighter than on the receding side.

Jet can be expressed as a series of blobs. But the number of blobs observed scales as the Doppler factor, such that for jets:

$$\frac{S_1}{S_2} = \left(\frac{1 + \beta\cos\phi}{1 - \beta\cos\phi}\right)^{2-\alpha} \tag{6.50}$$

One sidedness of jets is a relativistic effect!

Jet One-Sidedness, II

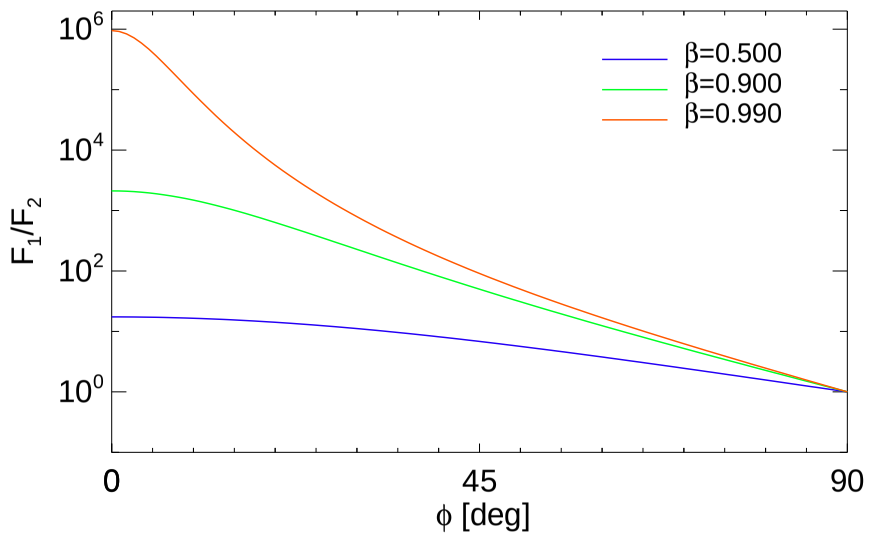

Kinematics of Relativistic Jets

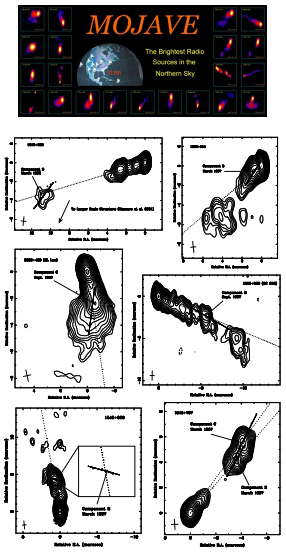

- **MOJAVE**: **M**onitoring **O**f **J**ets in **A**ctive galactic nuclei with **V**LBA **E**xperiments; (Lister et al., 2009)
- Wavelength $\lambda = 2$ cm (15 GHz)
- Statistically complete sub-sample: All flat-spectrum ($\alpha < 0.5$) sources whose compact flux density ever reached 1.5 Jy (2 Jy for southern sources)
- Extended sample includes all known gamma-ray blazars (newly detected *Fermi* sources added since 2009)
- Results, images and movies at
  `http://www.physics.purdue.edu/astro/MOJAVE/`
- Observing strategy optimized for each individual source (fast sources are observed every month, slower sources less frequently)

Survey and monitoring of extragalactic jets on parsec scales with the VLBA since 1995

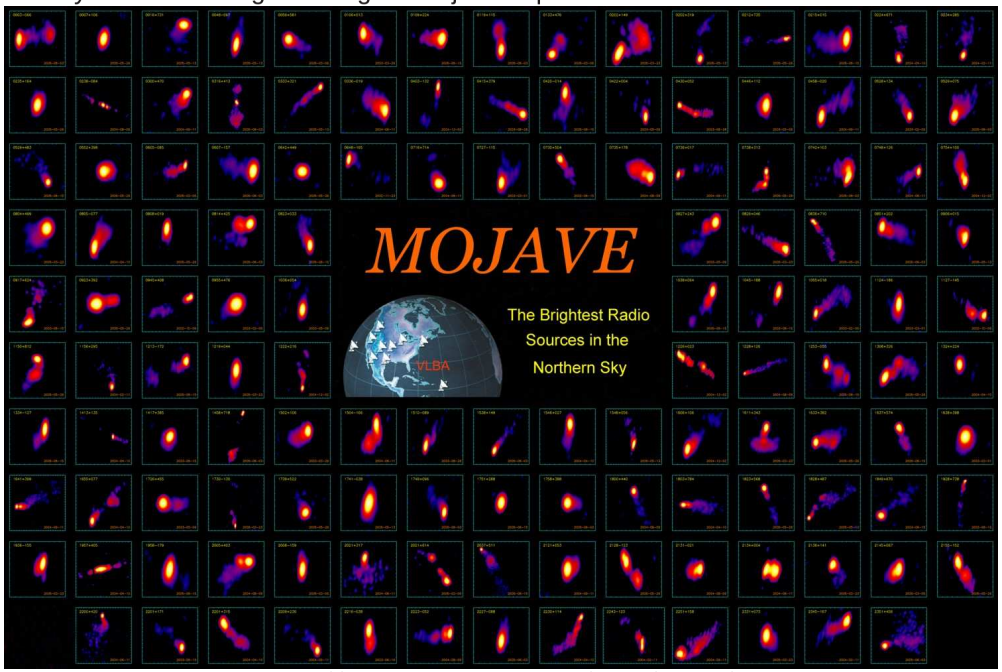

http://www.physics.purdue.edu/astro/MOJAVE/

Kinematics of Relativistic Jets

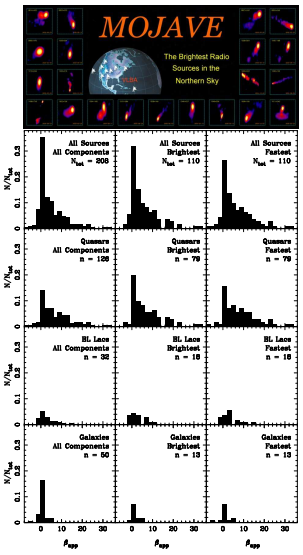

MOJAVE Results:

- Distribution of observed velocities typically between 0 and 15c: Quasars: tail up to $\beta_{\rm app} \sim 50$; BL Lacs and galaxies: mainly $\beta \lesssim 6$
- In the same jet, different components tend to have similar speeds; but there are exceptions
- In many sources, bent trajectories are seen, which do not back-extrapolate to the core: no cannon-balls!
- Observed pattern speed does not necessarily agree with beam speed
- Most of the flux-density originates in still unresolved regions smaller than 0.05 mas
- High-energy (gamma-ray) emitters have faster and more compact jets

(Kellermann et al., 2004; Kovalev et al., 2005; Cohen et al., 2007)

Cohen, M. H., Cannon, W., Purcell, G. H., Shaffer, D. B., Broderick, J. J., Kellermann, K. I., & Jauncey, D. L., 1971, ApJ, 170, 207

Cohen, M. H., Lister, M. L., Homan, D. C., Kadler, M., Kellermann, K. I., Kovalev, Y. Y., & Vermeulen, R. C., 2007, ApJ, 658, 232

Högbom, J. A., 1974, A&AS, 15, 417

Kadler, M., Ros, E., Lobanov, A. P., Falcke, H., & Zensus, J. A., 2004, A&AS, 426, 481

Kadler, M., et al., 2008, ApJ, 680, 867

Kameno, S., Sawada-Satoh, S., Inoue, M., Shen, Z.-Q., & Wajima, K., 2001, PASJ, 53, 169

Kellermann, K. I., et al., 2004, ApJ, 609, 539

Kovalev, Y. Y., et al., 2005, AJ, 130, 2473

Laing, R. A., & Bridle, A. H., 1987, MNRAS, 228, 557

Lister, M. L., et al., 2009, AJ, 137, 3718

Nilsson, K., Pursimo, T., Sillanpää, A., Takalo, L. O., & Lindfors, E., 2008, A&A, 487, L29

Ryle, M., Elsmore, B., & Neville, A. C., 1965, Nature, 205, 1259

Shu, F. H., 1991, The Physics of Astrophysics, Vol. I. Radiation, (Mill Valley, CA: University Science Books)

Whitney, A. R., et al., 1971, Science, 173, 225

Yang, J., Gurvits, L. I., Lobanov, A. P., Frey, S., & Hong, X.-Y., 2008, A&AS, 489, 517

Zensus, J. A., 1997, ARA&A, 35, 607